A Multiscale Numerical Study of Hurricane Andrew (1992). Part VI: Small-Scale Inner-Core Structures and Wind Streaks

M. K. YAU

Department of Atmospheric and Oceanic Sciences, McGill University, Montreal, Quebec, Canada

YUBAO LIU

National Center for Atmospheric Research, Boulder, Colorado

DA-LIN ZHANG

Department of Meteorology, University of Maryland, College Park, College Park, Maryland

YONGSHENG CHEN

Department of Atmospheric and Oceanic Sciences, McGill University, Montreal, Quebec, Canada

(Manuscript received 2 April 2003, in final form 6 January 2004)

ABSTRACT

The objectives of Part VI of this series of papers are to (a) simulate the finescale features of Hurricane Andrew (1992) using a cloud-resolving grid length of 2 km, (b) diagnose the formation of small-scale wind streaks, and (c) perform sensitivity experiments of varying surface fluxes on changes in storm inner-core structures and intensity.

As compared to observations and a previous 6-km model run, the results show that a higher-resolution explicit simulation could produce significant improvements in the structures and evolution of the inner-core eyewall and spiral rainbands, and in the organization of convection. The eyewall becomes much more compact and symmetric with its width decreased by half, and the radius of maximum wind is reduced by ~10 to 20 km. A zone of deep and intense potential vorticity (PV) is formed at the edge of the eye. A ring of maximum PV is collocated in regions of maximum upward motion in the eyewall and interacts strongly with the eyewall convection. The convective cores in the eyewall are associated with small-scale wind streaks.

The formation of the wind streaks is diagnosed from an azimuthal momentum budget. The results reveal small-scale Lagrangian acceleration of the azimuthal flow. It is found that at the lowest model level of 40 m, the main contributor to the Lagrangian azimuthal wind tendency is the radial advection of angular momentum per unit radius. At an altitude of 1.24 km, vertical advection of the azimuthal wind, in addition to the radial advection of angular momentum per unit radius, plays important roles.

Results of a series of sensitivity tests, performed to examine the impact of several critical factors in the surface and boundary layer processes on the inner-core structures and the evolution of the hurricane intensity, are presented.

1. Introduction

Considerable progress has been made in recent years in simulating hurricanes using high-resolution mesoscale models (e.g., Liu et al. 1997, hereafter LZY97; Wang 2002a; Braun 2002). In particular, LZY97 successfully simulated Hurricane Andrew (1992) employing a nested-grid (54/18/6 km) version of the fifth-generation Pennsylvania State University–National Center for Atmospheric Research (PSU–NCAR) nonhydrostatic Mesoscale Model (i.e., MM5). Their 72-h simulation covers the stage of rapid deepening, when the storm intensified from a tropical storm to a category-5 hurricane, and the stage of landfall over Florida.

As verified against various observations and the best track analysis, the model captures reasonably well many of the inner-core structures of the storm. In particular, the track, the explosive deepening rate (>1.5 hPa h^{-1}), the minimum surface pressure of 919 hPa preceding landfall, and the strong surface wind (>65 m s^{-1}) near the shoreline are well reproduced. Many kinematic, thermodynamic, and precipitation structures in the core regions simulated by the model bear strong resemblance

Corresponding author address: Dr. M. K. Yau, Department of Atmospheric and Oceanic Sciences, McGill University, Montreal, QC H3A 2K6, Canada.
E-mail: peter.yau@mcgill.ca

to previous observations of hurricanes. This successful simulation formed the basis for a series of subsequent diagnostic studies. Liu et al. (1999) analyzed the results of LZY97 to deduce the kinematic and thermodynamic structures of a hurricane. They performed an azimuthal average to obtain the axisymmetric structures and found that the airflow is characterized by a main inflow (outflow) in the boundary layer (upper troposphere), a divergent slantwise ascent in the eyewall, a penetrative dry downdraft at the inner edge of the eyewall, and a generally weak subsiding motion in the eye. A temperature inversion was found in the eye at an altitude of about 2–3 km. The inversion divides the eye into two parts, with a deep layer of warm/dry air above and a shallow pool of warm/moist air below. Other diagnostic studies led to an improved understanding of the vertical forcing dynamics in the eye and eyewall (Zhang et al. 2000), an explanation of the supergradient flow (Zhang et al. 2001), and insight into the thermodynamic budget of the hurricane (Zhang et al. 2002).

Although very encouraging results were obtained in LZY97, it is recognized that a grid size of 6 km is still too coarse to resolve some important features. For example, the size of the eye and the width of the eyewall are too large in the simulation. The model does not produce the many very finescale spirals found in recent radar measurements of intense hurricanes reported by Gall et al. (1998). The existence of small-scale jet streaks, inferred from an after-storm damage analysis of Hurricane Andrew by Wakimoto and Black (1994), were not well resolved. Moreover, some recent studies have pointed out that the inner-core structures, the thermodynamics of the eye and the eyewall, as well as the properties of spiral rainbands, can affect the maximum potential intensity and intensification of hurricanes (Barnes and Powell 1995; Holland 1997; Emanuel 1997; Willoughby 1998). Therefore, it is desirable to extend the results of our 6-km run to higher resolutions.

This paper extends the results of a 72-h multiscale simulation of Hurricane Andrew in LZY97 to include explicit simulation of convection and rainbands in the inner-core region (radius $<$200 km) employing a cloud-resolving grid size of 2 km. Sensitivity experiments will also be performed to examine the impact of several critical factors in the surface and maritime boundary layer (MBL) processes on the inner-core structures and the evolution of the hurricane. As will be shown, the use of better model physics, improved initial and boundary conditions, as well as high-resolution terrain and land use data, allows the 2-km model to simulate much more realistically the inner-core structures of the storm. The explicitly resolved convection in the core region, in turn, provides an opportunity to study the mechanism of vortex-convection interaction, especially on the formation of small-scale wind streaks. We shall compare the evolution of the finescale features from the simulation against the 6-km model and recent observations, including the evolution of the potential vorticity (PV) field which has been shown to be related to the development of vortex Rossby waves and convective rainbands in the inner-core of hurricanes (Guinn and Schubert 1993; Montgomery and Kallenbach 1997; Chen and Yau 2001). An azimuthal momentum budget will be computed to shed light on the formation of small-scale wind streaks.

The organization of the paper is as follows. Section 2 describes briefly the modeling methodology. Section 3 presents an analysis of the inner-core structures of the simulated storm, especially the eye, eyewall, and spiral rainbands. These structures are compared with available observations and the results from a coarser-resolution (6 km) run. An examination of the PV structure in the inner core is given in section 4. Section 5 contains the azimuthal momentum budget relevant to the formation of small-scale wind streaks revealed in the 2-km model. Sensitivity experiments are described in section 6. A discussion forms the subject of section 7. A summary and conclusions are given in the final section.

2. Model description

We employ a version of the PSU–NCAR MM5 similar to that described in LZY97. However, we use (a) the more recent MM5 code (version 2.9), (b) the hail version of the National Aeronautics and Space Administration Goddard Space Flight Center (NASA Goddard) microphysical parameterization, which allows realistic simulation of heavily rimed graupel particles in strong convective updrafts (Tao and Simpson 1993), (c) the U.S. Navy PBL parameterization based on turbulence kinetic energy (TKE) and a 2.5-order closure (Burk and Thompson 1989), and (d) no shallow convection scheme.

The initial and boundary conditions of the high-resolution 2-km model are constructed from the hourly output during the last 12 h of the 72-h coarser resolution (18/6 km) runs which in turn are affected by the bogus vortex in a 54-km model grid described in LYZ97. It is recognized that there are more recent vortex initialization techniques, including the work of Zhu et al. (2002) using Advanced Microwave Sounding Unit (AMSU) data, and the four-dimensional variational data assimilation (4DVAR) work of Pu and Braun (2001). The advantage of the bogus vortex technique of LZY97 is that the methodology does not produce any notable ''shocks'' once the model is integrated, since all the meteorological fields in the tropical easterlies are relatively uniform and since the same model is used in constructing the bogus vortex so that the vertical circulation structures so generated tend to be more compatible with the model dynamics and with the initial larger-scale conditions than other vortex bogus techniques. The limitation of the LZY97 technique is that it works only if the storm travels approximately parallel to a latitude circle with no large change in the Coriolis parameter. Furthermore, the size of the bogus vortex

may be larger than the actual vortex because of the coarse resolution involved in its construction. We should point out that there is ample time for the model to adjust to the bogus vortex which was inserted 4.5 days before the time period of the high-resolution 2-km simulation.

To alleviate the problems associated with the lateral boundaries, a two-way nested mode (6/2 km) was selected for the high-resolution run. Figure 1 shows the model domain, mesh structure, and the terrain and land use distribution. The terrain height was interpolated from the Defense Mapping Agency 30-s. terrain dataset and the surface property was taken from the standard PSU–NCAR 10-min land use dataset. To simulate accurately the landfall process, we also corrected the errors in the storm track and in the coastline described, respectively, in LZY97 and Zhang et al. (1999) in the new initial conditions. Both the 6- and 2-km meshes consist of 232 $\times$ 169 $\times$ 23 points in (x, y, σ) coordinates, covering areas of 1386 km $\times$ 1008 km and 462 km $\times$ 336 km, respectively. The fine mesh is moved every 3 h so the inner-core of the hurricane is within the central region of the domain. The model is integrated for 12 h, from 0000 to 1200 UTC 24 August 1992. This period covers the final fast-deepening stage and the landfall stage over Florida.

For conciseness, we will focus only on the final deepening stage of Andrew in this paper. The landfall stage over Florida will be the subject of a future publication.

3. Structure of the eye, eyewall, and rainbands

We should first mention that the 2- and the 6-km simulations yield similar results in terms of the central pressure and the vortex-scale structures of the hurricane. However, many finer-scale features in the higher-resolution simulation show better agreement with radar and other observations, especially within a radius of 100 km of the inner-core region.

a. Radar reflectivity

Figure 2 compares the observed radar reflectivity to the simulated reflectivity from the 2- and 6-km models at 0740 UTC 24 August 1992, about 2 h before landfall. The models simulate a circular eye and a compact circular eyewall, embedded within are well-resolved convective bands. Although the size of the eye is similar in the two runs, the width of the eyewall is reduced by $\sim$10 km in the 2-km mesh (Fig. 2b), a significant improvement as verified against radar observations (Fig. 2c). Note that in the 2-km model, a patch of maximum reflectivity lies in the southern eyewall while it is located to the north in the observations. This is just a transient propagating feature as the storm is rotating rapidly. Outside the eyewall, the structures of the simulated small-scale spiral rainbands are similar to those observed in tropical cyclones. For example, Gall et al. (1998) uncovered finescale bands spiralling around the center of Hurricane Andrew using correlation techniques. They speculated that these bands might be related to small-scale wind peaks that caused some of the worst damage by the hurricane. Figure 2b also shows a small amount of precipitation associated with stratus and stratocumulus clouds in the eye below the temperature inversion, a feature which was also observed (cf. Figs. 2b and 2c).

To examine the structure of convection in the eyewall, we plot in Fig. 3 west–east vertical cross sections of radar reflectivity through the hurricane center. As shown, the eyewall is composed of strong convective entities sloping outward with height. Some finescale steps, associated with downdrafts, appear in the simulated radar reflectivity at the inner edge of the eyewall. A number of inner convective bands can be seen. In the 2-km run (Fig. 3b), the width of the simulated bands is $\sim$15 km with a spacing of $\sim$20 km. Their number, dimension, and spacing are more realistic in the higher-resolution experiment (cf. Figs. 3a and 3b), as verified against the Miami radar RHI observations (Fig. 3c). In agreement with radar observations, the radar reflectivity in the eyewall decreases in intensity above the freezing level, although the rate of decrease is slower in the 2-km run.

b. Kinematic structure

With the eyewall convection and the spiral rainbands better resolved, the 2-km model is able to simulate important disturbances embedded in the violent swirling winds. Figure 4 presents the surface ($z \approx 40$ m) winds in the 2-km model approximately every 2 h from 0720 to 1100 UTC 24 August. The winds in the eyewall are stronger than those from the 6-km model (not shown). This increase in wind speed is attributable to the increase of radial pressure gradient in the eyewall [or the decrease in the radius of maximum wind (RMW)] since the central pressures are similar in the two cases. In contrast, within the eye, the pressure gradient of the 2-km model is much weaker, causing the winds to decrease exponentially from the eyewall inward. The exponential variation differs significantly from the near linear reduction in the 6-km model. Using aircraft flight-level data, Kossin and Eastin (2001) showed that in intensifying hurricanes, the tangential winds decrease exponentially toward the eye. However, after maximum intensity is reached, there is a linear variation of the tangential wind in the eye as a result of vorticity mixing (Schubert et al. 1999). Thus, solid-body rotation may be inappropriate to characterize the winds in the eye during the intensifying stage. Also relative to the 6-km model, the air in the eyewall in the 2-km model possesses a larger rotational inertia, so the secluded air mass in the eye would be better protected from dilution by entrainment and mixing of environmental air.

Although the 2-km model produces a more symmetric eye and eyewall relative to the 6-km run, stronger per-

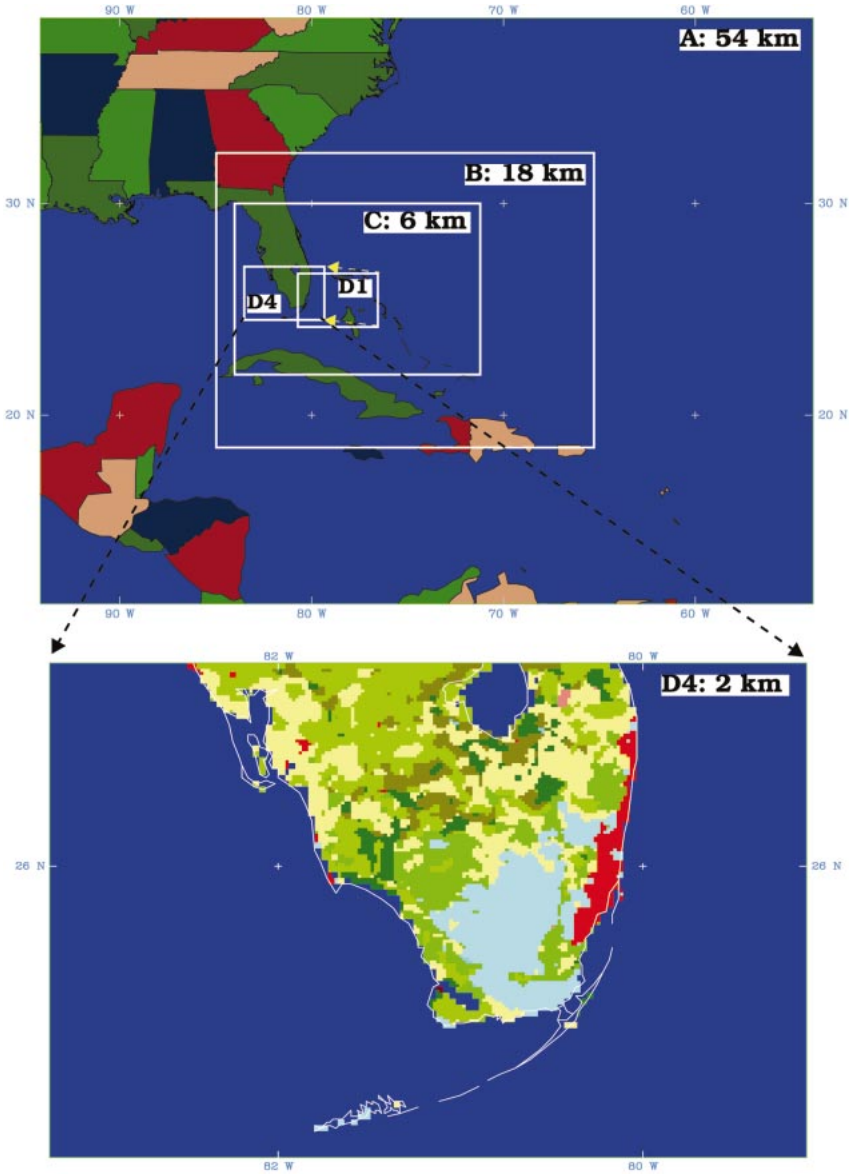

FIG. 1. Configuration of domains. Domains A and B are the same as A and B2 in LZY97. The initial conditions for domains C and D1, valid at 0000 UTC 24 Aug 1992, are constructed from the control simulation in the same paper. The 2-km model domain D is moved once every 3 h during the 12-h simulation from D1 to D4 (D2 and D3 not shown). (bottom) The land use of D4 is depicted.

turbations occur in the circulation in association with more intense and more numerous convective cells. Figure 4 shows the development of wind streaks in the eyewall regions, with magnitudes of >15 m s^{-1} relative to the surrounding areas, widths of $\sim$10 km, and azimuthal lengths of a few tens of kilometers. The wind streaks always exist when the storm is over the ocean (Fig. 4a), during (Fig. 4b), and after landfall (Fig. 4c), with two to three local maxima frequently observed across the eyewall. During the landfall, however, both the vortex-scale swirling winds and the small-scale wind streaks weaken considerably (Figs. 4b,c). These small but intense features have been reported in the literature from an after-storm damage analysis of Hurricane Andrew by Wakimoto and Black (1994). Powell et al. (1991) also suggested that such small-scale enhanced wind disturbances existed in the eyewall of Hurricane Hugo (1989).

LZY97 showed a favorable agreement of the modeled surface winds at landfall as compared to the composite analysis of Powell and Houston (1996). Zhang et al. (1999) elaborated further on several detailed structures of the surface winds. With the storm track corrected, and the use of high-resolution terrain and land use data,

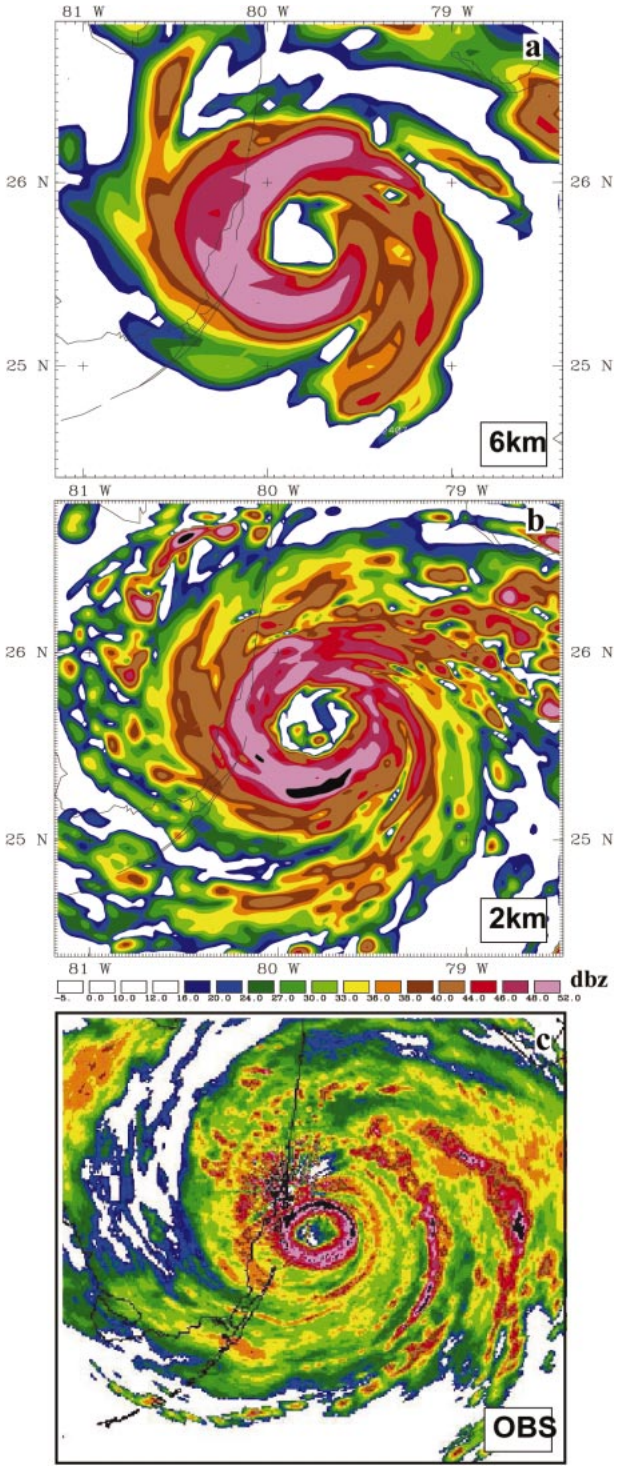

FIG. 2. Surface radar reflectivity (dBZ) distribution, valid at 0740 UTC 24 Aug in (a) the 6-km model, and the (b) 2-km model. (c) The Miami radar image just before Andrew's landfall. Same color shadings are used for (a)–(c).

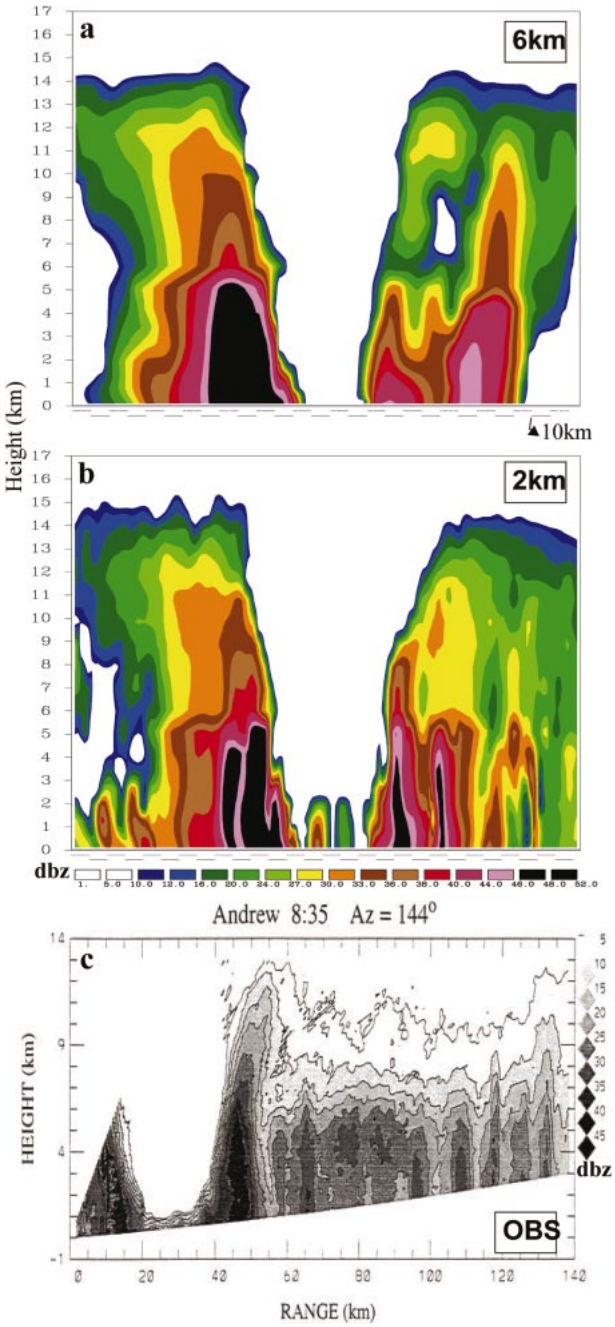

FIG. 3. Same as in Fig. 2 but for west–east vertical cross sections of (a) the 6-km model, and (b) 2-km model through the centers of the hurricane. (c) The Miami radar RHI observation at 0835 UTC looking toward the southeast (courtesy of Gall et al. 1998).

the 2-km model simulates much more realistically the structure of the surface winds during landfall. In particular, Fig. 4b indicates that the wind decreases rapidly over land, with a speed of 50–55 m s^{-1} in the front eyewall region over land and >60 m s^{-1} in the rear eyewall region over ocean. A wind streak with a speed of 65 m s^{-1} can be located in the southwestern portion

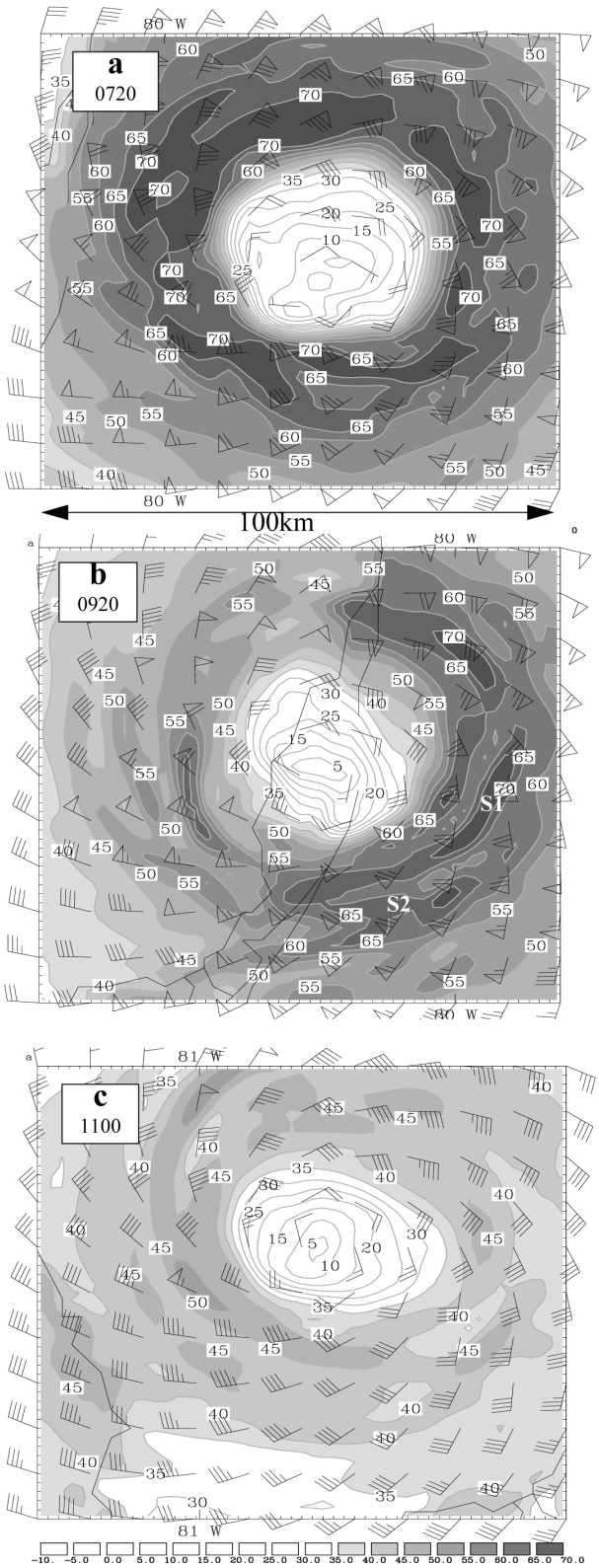

FIG. 4. The surface winds of Andrew in the 2-km model at (a) 0720, (b) 0920, and (c) 1100 UTC 24 Aug 1992. Units: m s^{-1}.

of the eyewall over the Corel Reef region, where strong gusts >70 m s^{-1} were reported at several locations (Mayfield et al. 1994) and damages corresponding to the F2–F3 Fujita scale were recorded by Wakimoto and Black (1994). Over the ocean, several wind streaks of 70–75 m s^{-1} occur within the eyewall. Another improvement of the high-resolution model is the better representation of the transition zone of the winds in the coastal regions. The 2-km model tends to have a narrower width of the transition zone than that from the 6-km model.

Figure 5 shows the azimuth–height cross section of the tangential winds and the in-plane relative flow vectors in the eyewall. The locally enhanced wind maxima occur throughout the lower troposphere with some organized structures. However, there is large variability of the wind structure at different levels. The winds in the eyewall region change rapidly in the lowest 2 km due to the presence of surface friction. At times, the speed increases by as much as 30 m s^{-1} from the surface to 0.6–0.9 km. It then decreases upward, forming a unique wind jet at around 1-km height. Evidently, any vertical motion crossing the jet will cause a large vertical transfer of horizontal momentum, generating strong disturbances of the local winds. The in-plane wind vectors indicate that some local wind maxima are associated with upward motion and hence convection (e.g., see the west-northwest sector in Fig. 5a). However, the mechanism for the interaction between eyewall convection and small-scale wind disturbances remains unclear. We will present in section 5 the azimuthal momentum budget to shed light on the formation of these wind streaks.

Liu et al. (1999) presented a conceptual model of the circulation and thermodynamic structure in the inner-core region of intense mature hurricanes based on the results of the 6-km model. It is of interest to compare the current 2-km model with these results. An inspection of the radius–height cross sections of the azimuthally averaged tangential and radial winds (not shown) shows that they are similar to those in Liu et al. (1999) and Zhang et al. (2001). Even though the equivalent potential temperature (θ_e) and the vertical winds are comparable in overall structures to the 6-km model, there are differences in small-scale structures in the eyewall worthy of note.

Most significantly, the eyewall updraft (Fig. 6a) is more concentrated. For example, its width of 10 km is about half, and its maximum intensity of 3.5 m s^{-1} at $z = 7$ km is about one-third more than that in the 6-km model (see Fig. 8 in Liu et al. 1999). A lower-level maximum, with a magnitude as strong as 1.6 m s^{-1}, protrudes into the eye in the MBL below 1.5 km. This protruded updraft is a common feature in the simulation and causes the formation of stratus clouds which often become attached to the eyewall in the low level. Similar to the 6-km run, a deep narrow dry downdraft (DD) zone is located along the inner edge of the eyewall. In the outer regions (i.e., $R > 70$ km), the 2-km model

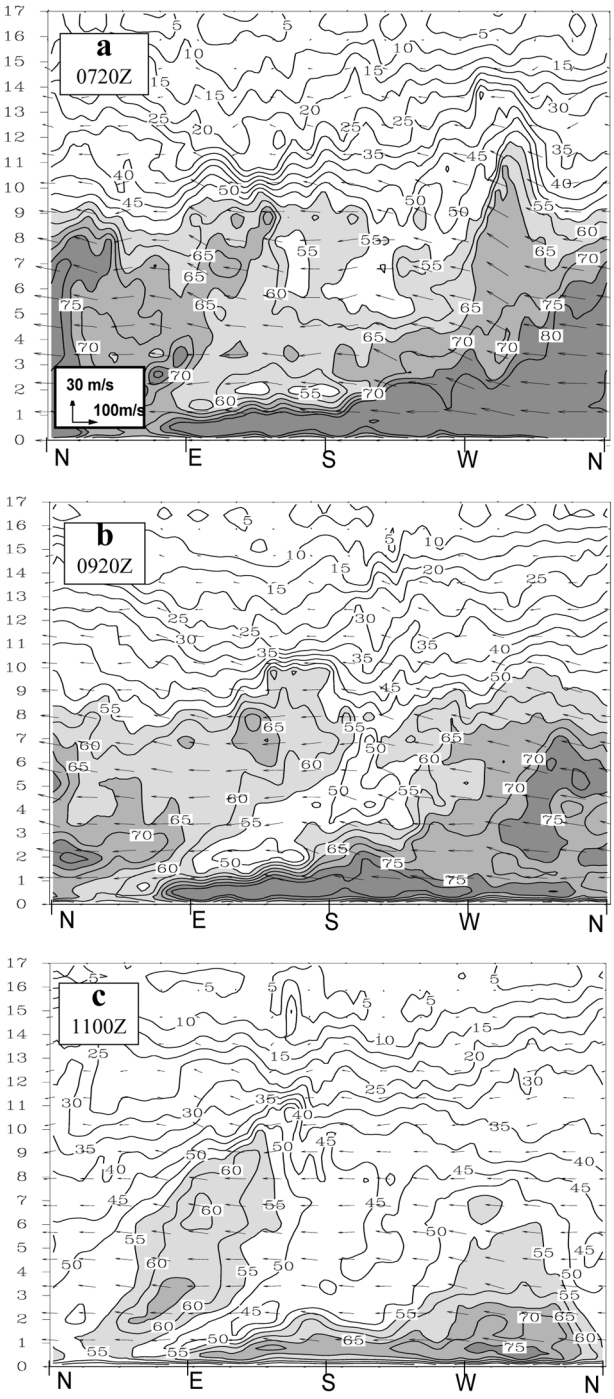

FIG. 5. Same as in Fig. 4 but for azimuth vertical cross sections in the eyewall, sloping from a radius of 28 km at the surface to 58 km at a height of 17 km.

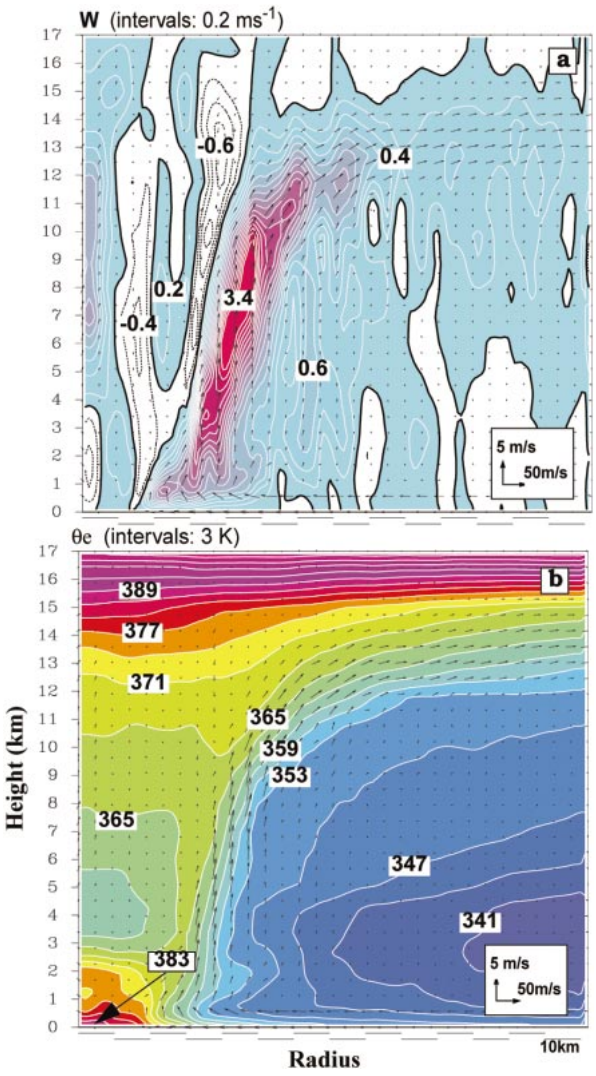

FIG. 6. Radial–height sections of the azimuthally averaged fields valid at 0720 UTC 24 Aug 1992: (a) vertical velocity W, and (b) equivalent potential temperature θ_e. In-plane circulation vectors are superposed.

clearly shows dominant descending motion below the melting level, resembling Doppler radar analysis of Hurricane Alicia given in Marks and Houze (1987). The wavy vertical motion structure in the upper outflow layer is indicative of inertial gravity waves and may be caused by the use of too coarse vertical resolutions (see Zhang and Wang 2003).

The mean thermodynamic structure (Fig. 6b) in the 2-km model also exhibits some significant changes. The high θ_e funnel located at the inner edge is better defined. The in-plane circulation vectors indicate downward transport of high θ_e air from the tropopause by the DDs and upward transport from the bottom of the eye (see Zhang et al. 2002). Of particular interest is that the θ_e maximum, which was located at the surface near the center of the eye in the 6-km model, is now located at around a radius of about 9 km, forming a ring of large θ_e. This high θ_e ring may lead to the development of stratocumulus in the eye below the inversion (cf. Fig. 2b) as a result of strong potential instability. Kossin and Eastin (2001) demonstrated from a two-dimensional

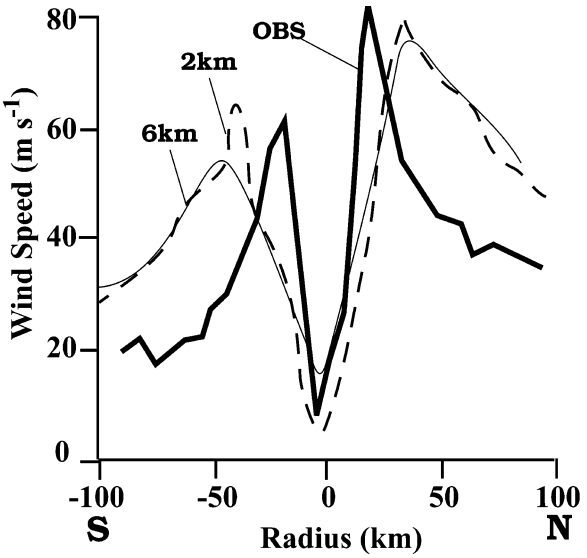

FIG. 7. Comparison of the south–north wind profiles between the aircraft observations [thick solid, reproduced from Willoughby and Black (1996)], 6-km model simulation (thin solid from LYZ97), and 2-km simulation (dashed line) at an hour before landfall.

barotropic model that the eyewall high θ_e air, in the form of passive tracers, can enter the eye from the eyewall as a result of vorticity mixing (Schubert et al. 1999). They stated that ''On entering the eye, the tracers formed swirling patterns that were remarkably similar to low cloud patterns often observed in the eyes of intense hurricanes.''

Figure 7 compares the simulated tangential wind profile to the wind observations reported by Willoughby and Black (1996) along the aircraft flight legs an hour before landfall. Also included is the one from the 6-km model simulated by LZY97. Clearly the 2-km model reproduces better the wind distribution in terms of the RMW, the slope (radial gradients) of the wind profile, and the weak winds observed near the central region of the eye. In particular, the RMW is reduced by 10–20 km, but is still too large by 20–25 km.

c. *Small-scale spirals*

In situ observations in Hurricane Hugo obtained by the National Oceanic and Atmospheric Administration (NOAA) WP-3D aircraft at an altitude of 3.5 km indicated small-scale spiral bands that were characterized by strong ascending cores with maximum vertical velocities of 3–5 m s^{-1} (Gall et al. 1998). The cores are associated with maxima in θ_e and cloud water content. Figure 8 shows horizontal distributions of the vertical velocity at various heights at 0700 UTC. In spite of the

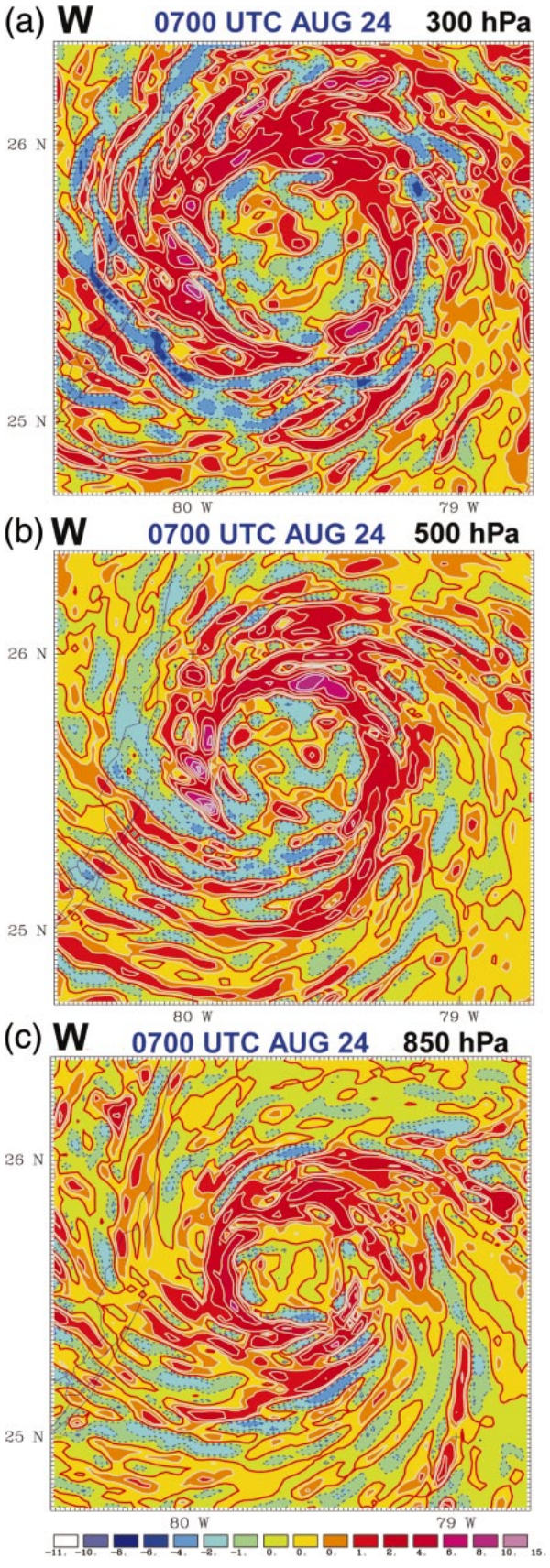

→

FIG. 8. Vertical velocity in m s^{-1} valid at 0700 UTC 24 Aug from the 2-km model at (a) 300, (b) 500, and (c) 850 hPa.

well-organized primary and secondary circulations, the vertical motion in the whole core region is composed of small-scale spirals, which are, on average, about 5–10 km wide and 20- to over a 100 km long. They exhibit a wavy pattern in the radial direction with interweaving ascending and descending zones. The more dominant ascending bands appear to swirl inward, merging with the eyewall to form a circular updraft zone where the strongest convection is concentrated.

Strong asymmetries developed in the eyewall coinciding with the presence of spiral rainbands. Moving radially outward across the eyewall, one encounters two or more strong convective bands, sometimes with weak descending zones in between. The eyewall bands tend to be stretched in the tangential direction by the strong swirling winds. The embedded convective cores are oval-shaped, with their major axis oriented along the direction of the connecting spirals. The maximum vertical velocity in the ascending cores often exceeds 10 m s^{-1}. The pattern and the scale of the convective cores and bands are similar to those of the horizontal wind perturbations (Fig. 4), suggesting a linkage between the convective cores and the violent wind streaks at the surface.

Despite the strong updrafts, there is an absence of a one-to-one relationship between radar reflectivity and vertical velocity (cf. Figs. 2 and 8). This may be caused by the rapid rotation of the convective disturbances and also by the fact that reflectivity is an integrated quantity of the hydrometeors but local vertical motion is determined by latent heat release. However, the shape, size, and period of the spirals are in excellent agreement with those from Andrew obtained by Gall et al. (1998) using radar correlation techniques at about the same time. Although the primary variable used in their analysis is radar reflectivity, they reported that small-scale spiral bands were only faintly visible in the radar images but showed up much better in the perturbation reflectivity fields. The striking similarity between the modeled spiral updrafts (Fig. 8) and the spirals of radar reflectivity perturbations and correlation fields depicted in Figs. 5–6 of Gall et al. (1998) supports their speculation that small-scale, strong ascending/descending spiral bands exist in the core region of hurricanes, at least in the strong ones like Andrew.

Figure 8 also indicates that the vertical motion spirals appear throughout the deep troposphere with their intensities increasing with height until about 300 hPa. Downdrafts are also common in the eyewall, but they are weaker in intensity and fewer in number than updrafts. They can be a few kilometers deep and up to 20 km wide. In the MBL, the up and down spirals are well defined. However, only very weak vertical motion occurred with the exception of three major bands at about 1 m s^{-1} in their up/down vertical speed (not shown). The vertical motion increases to 2–4 m s^{-1} at 850 hPa, and more than 10 m s^{-1} above 500 hPa. The strongest upward motion is located at 300 hPa above which level the outflow from the eyewall occurs.

Liu et al. (1999) found that the eye in the 6-km model is characterized by very weak (few cm s^{-1}) mean-descending motion, but with strong (up to ± 1 m s^{-1}) instantaneous gravity wave oscillations located in the region also. The strongest descending motion is located right along the inner edge of the eyewall. Figure 8 indicates that the 2-km model supports these findings but with additional details. Specifically, the eye contains small-scale, less-organized disturbances with maximum vertical motion up to several m s^{-1}. On average, their life cycle is about 20–30 min, similar to the vertical motion cores in the eyewall and spiral bands. Intense descending cores, with a magnitude of $\sim$2 m s^{-1}, are found right inside the eyewall updrafts. Note also the significant descending motion between the eyewall and the spiral rainbands. These intense descents correspond to the organized dry-downdraft zone found in the 6-km model except that they possess a narrower radial width. It should be pointed out that in general, the distribution and magnitude of the vertical motions bear excellent agreement to Doppler radar observations in Hurricane Norbert (1984) reported by Marks et al. (1992).

d. Thermodynamic effects of the spirals

Condensation occurs in the outer small-scale upward motion spirals and the strong convective cores in the eyewall. Figure 9 shows a strong correlation between the cloud water content (Qc) and the vertical motion (W) in these regions. The largest Qc of 2 g kg^{-1} is found in the eyewall at 500 hPa. In the outer spirals, Qc is smaller with values between 0.2 and 1.0 g kg^{-1}. In general, the cloud water in the spiral bands and eyewall are organized in cells, with their shape, orientation, and size closely matching those of the ascending cores. Typically 8–12 convective cells are located in the eyewall. Stronger cells appear preferentially in the northwest quadrant. On average, the maximum vertical velocity associated with the convective cells is around 6–8 m s^{-1} but can exceed 12 m s^{-1} in the strongest ones. Since the updraft maximum is located at around 7-km altitude, a level about 1.5 km above the freezing level, latent heat release from the freezing and sublimation processes may enhance the upward acceleration.

Because of the rapid evolution of the perturbed vertical motion, there can be a phase lag between W and Qc in some places, and some ascending air remains unsaturated, particularly for the relatively less humid outer regions (850 and 500 hPa). These features are consistent with NOAA's WP-3D reports in Hurricane Hugo (Gall et al. 1998).

The ascending motion in the spirals and eyewall transports a significant amount of energy from the ocean surface. Figure 10 shows that at 850 hPa, θ_e increases rapidly from the outer region toward the eye with asymmetries correlated with descending and ascending mo-

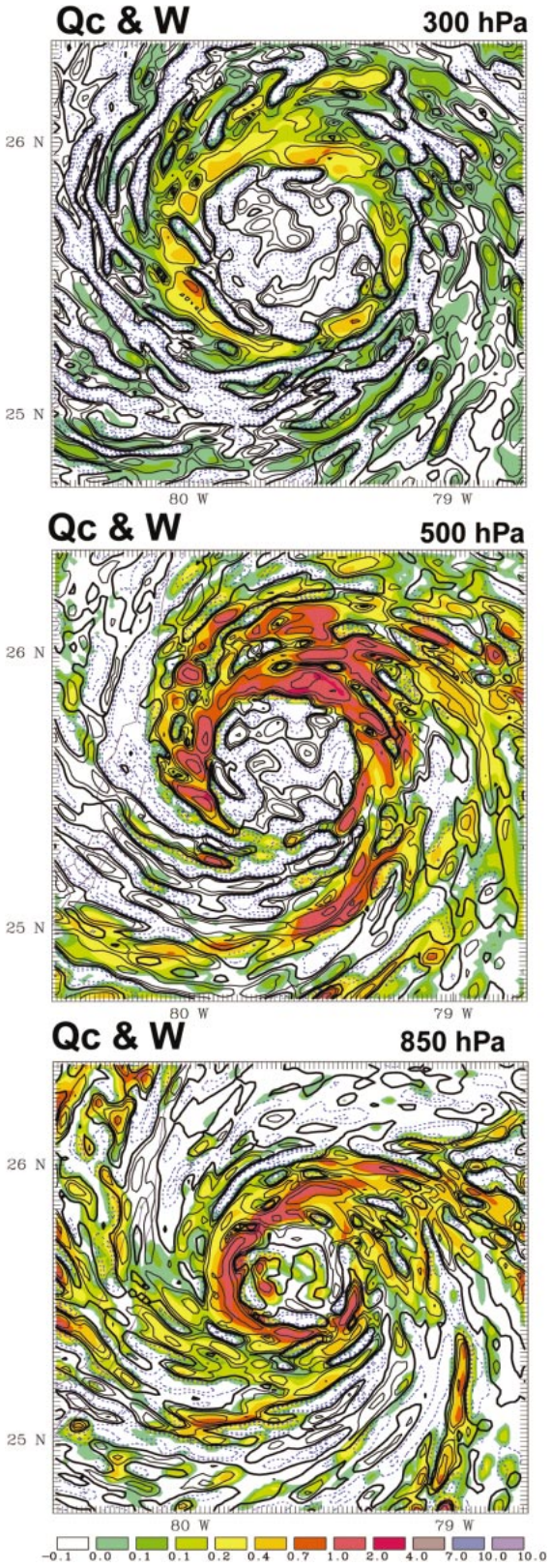

FIG. 9. Same as in Fig. 8 but for cloud content (sum of cloud water and cloud ice mixing ratios in g kg^{-1}, shaded). The superimposed contours are vertical velocities with the same contour interval as in Fig. 8. Thin solid lines, dashed lines, and thick solid line denote upward motion, downward motion, and zero velocity, respectively.

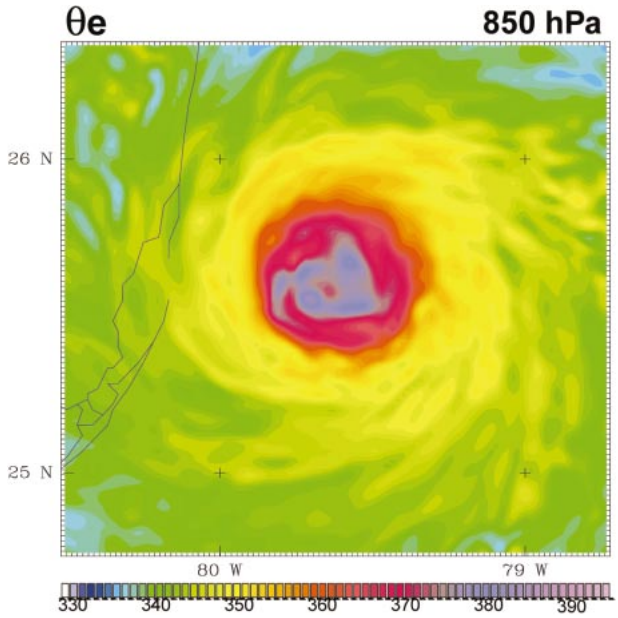

FIG. 10. Equivalent potential temperature (θ_e, K) at 850 hPa, valid at 0700 UTC 24 Aug 1992.

tions in the spirals. In the regions of strong spirals, the locally enhanced θ_e can reach values of 3–5 K relative to the surrounding air. As shown in Fig. 6b, the largest θ_e at the lower levels is not located at the eye center, but rather in a very irregular ring-shaped zone right inside the eyewall. The asymmetric spiral shape of the maximum θ_e ring suggests modulation of eyewall convection and strong interaction between the eyewall and the eye, consistent with the findings of Schubert et al. (1999) that vorticity mixing takes place between the hurricane's eye and eyewall region. Higher up, at 500 and 300 hPa, the maximum θ_e still occurs in a ring around the eyewall (not shown).

4. Inner-core PV structures

Spiral rainbands have long been viewed as gravity–inertia waves (e.g., Kurihara 1976; Willoughby 1978a,b). However, MacDonald (1968) suggested that they are ''Rossby-like'' waves possessing a countergradient momentum flux. More formal development of the theory of these waves in hurricanes came only recently. Guinn and Schubert (1993) derived the general conservation equation for wave activities applicable to rotating vortices in the context of shallow water dynamics. Montgomery and Kallenbach (1997) were the first to coin the term ''vortex–Rossby waves'' and to derive the

←

local dispersion relation for these waves including both azimuthal and radial wave propagation. They were also the first to demonstrate the ''countergradient'' properties of these waves on a monopolar vortex. Although both gravity waves and vortex Rossby waves should coexist in real hurricanes, recent observational analysis (Reasor et al. 2000) and numerical simulations using 3D primitive equation models (e.g., Chen and Yau 2001; Chen et al. 2003; Wang 2002a,b) show that inner spiral rainbands mainly exhibit characteristics of vortex Rossby waves. In particular, Chen and Yau (2001) showed that the interaction of low-level PV anomalies with boundary layer friction and the strong coupling of the PV band and condensation give rise to the inner spiral bands. They also verified that the propagation properties of these bands are consistent with predictions of vortex–Rossby wave theory.

While Chen and Yau (2001), and Wang (2002a) have shown PV structures in hurricane cores with a coarser grid size of 6 and 5 km, respectively, it is of interest to examine such structures in our 2-km model. Figure 11 depicts the horizontal distribution of Ertel's PV at 0700 UTC at 850 and 300 hPa. It is clear that PV is not uniform in the core of the hurricane but is marked by a ringlike structure. A comparison with the vertical motion (Fig. 8) indicates that the ring of maximum PV is located in regions of maximum upward motion in the eyewall. The outer region of the ring is characterized by numerous small-scale patches of positive and negative PV ($<\pm 5$ PVU). These patches are shredded from the PV ring surrounding the vortex center and are sheared horizontally in the shape of spirals, similar to the findings of Schubert et al. (1999). A careful inspection of the figure also indicates that in the inner region of the ring, patches of high PV are being mixed or transported into the eye region. Similar to the distribution of radar reflectivities, the radius of the PV ring increases with height, indicative of the outward slope of the eyewall with height.

Figure 12 shows a south–north vertical cross section through the central core of the vortex. In the 2-km model (Fig. 12b), the PV is distributed vertically in the shape of a bowl which extends up to 13 km in altitude. Large values are found along the side walls (where the eyewall is located) and the bottom (where the inversion in the eye is situated) of the bowl. Above and below the inversion in the eye, the values of PV are much smaller. This bowl-shaped PV structure persists in the azimuthal average (Fig. 12c). In comparison, the PV anomaly and the bowl structure in the 6-km model (Fig. 12a) are weaker and there are local patches of high PV anomaly in and above the MBL in the eye region. Near the model top, the strong static stability (see Fig. 6b) results in some high-valued PV patches.

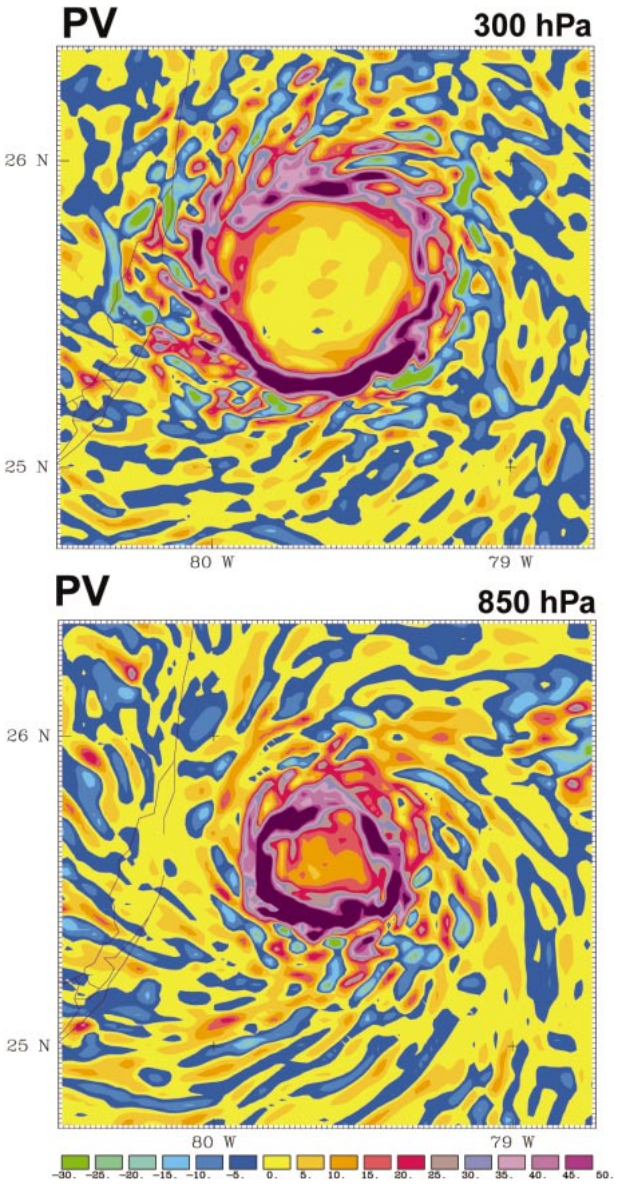

FIG. 11. Same as in Fig. 8 but for PV in units of PVU.

5. Azimuthal momentum budget

To understand the formation of the wind streaks depicted in Fig. 4, we compute the momentum budget using the following governing equation for azimuthal momentum in cylindrical coordinates (r, λ, z)

$$\frac{\partial v}{\partial t} + u\frac{\partial v}{\partial r} + \frac{v}{r}\frac{\partial v}{\partial \lambda} + w\frac{\partial v}{\partial z} + \frac{uv}{r} + fu - 2\Omega \cos\phi \sin\lambda w = -\frac{\alpha}{r}\frac{\partial p}{\partial \lambda} + F_\lambda, \qquad (1)$$

where u, v, and w are, respectively, the radial, azimuthal, and vertical winds relative to the earth. The parameters f, α, p, and ϕ denote the Coriolis parameter, specific volume, pressure, and latitude, respectively. Equation (1) can be rewritten as

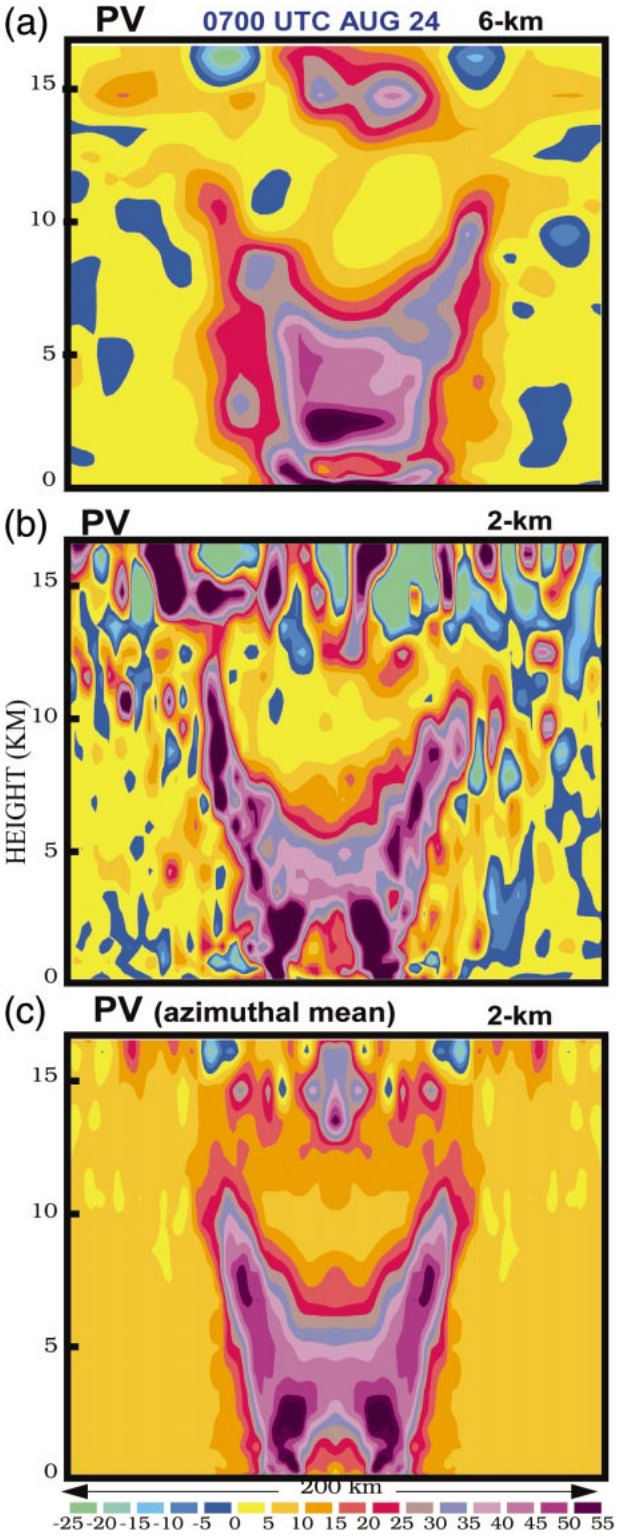

FIG. 12. South–north vertical cross section of PV through the center of the simulated hurricane in the (a) 6-km model and the (b) 2-km model, and (c) azimuthal mean PV in the 2-km model valid at 0700 UTC 24 Aug 1992.

$$\frac{\partial v}{\partial t} + \frac{1}{r}\frac{\partial\left(\frac{v^2}{2}\right)}{\partial\lambda} + w\frac{\partial v}{\partial z} + \eta_a u - 2\Omega\cos\phi\sin\lambda w = -\frac{\alpha}{r}\frac{\partial p}{\partial\lambda} + F_\lambda, \quad \text{or}$$

$$\underset{\text{VTOT}}{\left(\frac{\partial}{\partial t} + \frac{v}{r}\frac{\partial}{\partial\lambda}\right)v} = \underset{\text{VVA}}{-w\frac{\partial v}{\partial z}} \underset{\text{VVOR}}{-\eta_a u} + \underset{\text{VCOR}}{2\Omega\cos\phi\sin\lambda w} \underset{\text{VPGF}}{-\frac{\alpha}{r}\frac{\partial p}{\partial\lambda}} + \underset{\text{VFRIC}}{F_\lambda}, \tag{2}$$

with

$$\eta_a = \xi_a + \frac{1}{r}\frac{\partial u}{\partial\lambda} = f + \frac{1}{r}\frac{\partial(rv)}{\partial r},$$

where ξ_a is the vertical component of the absolute vorticity.

Equation (2) states that the quasi-Lagrangian azimuthal wind tendency (VTOT) is determined by the vertical advection (VVA), the radial absolute vorticity flux (VVOR) involving the relative vorticity of the azimuthal wind, the Coriolis force (VCOR), the azimuthal pressure gradient force (VPGF), and friction and diffusion (VFRIC). In the core region of hurricanes, f is much smaller than $(1/r)[\partial(rv)/(\partial r)]$; therefore VVOR $\approx -(u/r)[\partial(rv)/\partial r]$ and can be interpreted as the radial advection of angular momentum per unit radius.

Before presenting the analysis of Eq. (2), we first display in Fig. 13 the horizontal wind components, PV, ξ_a, η_a, and the PV generation rate by latent heating at $z = 1.24$ km which is above the MBL. Interested readers are referred to Liu et al. (1999) for a detailed description of the transformation between the MM5 (x, y, σ) and cylindrical coordinates. At 0630 UTC, the azimuthal winds (Fig. 13a) are quite symmetric within a radius of 20 km. However, asymmetries associated with small-scale wind streaks are located in an annulus 20–40 km from the center. The maximum azimuthal wind speed in some of the streaks exceeds 100 m s^{-1}. The pattern of the radial wind (Fig. 13b) indicates outflow (>50 m s^{-1}) relative to the earth in the southwest quadrant and weaker inflow in the northeast and northwest quadrants. It is known that in both the 2- and 6-km models, the azimuthally averaged radial wind relative to the storm exhibits an outflow jet just above the MBL (see Fig. 1b of Zhang et al. 2001). Thus, the inflow relative to the earth in Fig. 13b is the result of the asymmetry of the radial wind and the superposition of the motion of the storm (−8 m s^{-1}).

Figures 13c and 13d reveal that the distributions of PV and ξ_a are quite similar, indicating that ξ_a is the main contributor to PV. Also the similarity between ξ_a and η_a (cf. Figs. 13d and 13f) suggests that a large portion

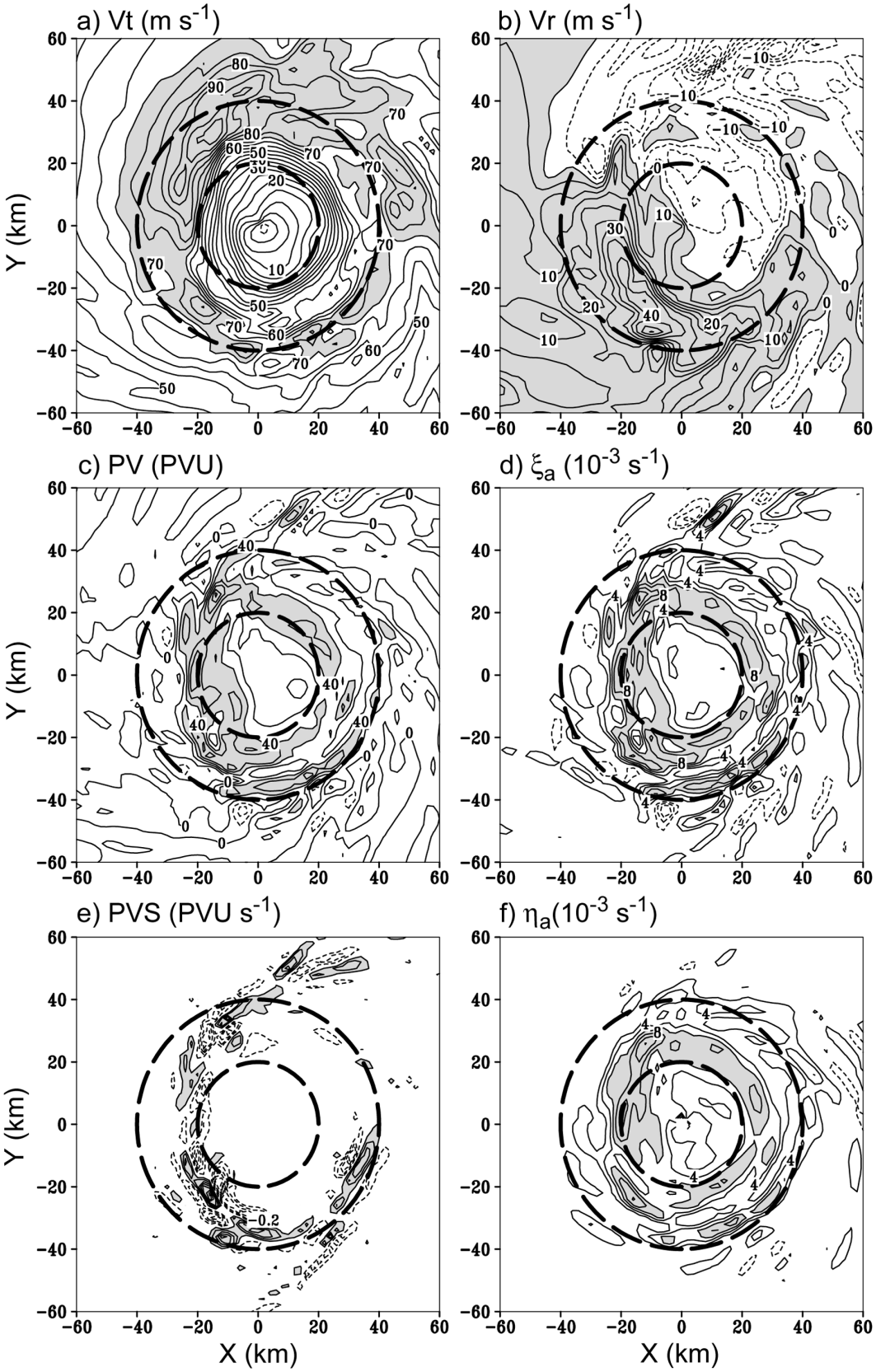
a) Vt (m s-1)
b) Vr (m s-1)
c) PV (PVU)
d) ξa (10-3 s-1)
e) PVS (PVU s-1)
f) ηa(10-3 s-1)
Y (km)
X (km)

of the absolute vorticity arises from the relative vorticity associated with the azimuthal wind. Therefore, we can write PV $= \alpha\boldsymbol{\eta}\cdot\boldsymbol{\nabla}\theta \approx \alpha\xi_a(\partial\theta/\partial z)$, with the absolute vorticity vector $\boldsymbol{\eta} = 2\boldsymbol{\Omega} + \boldsymbol{\nabla}\times\mathbf{V}$. It follows that

$$\frac{d\mathrm{PV}}{dt} \approx \left(\alpha\frac{\partial\theta}{\partial z}\right)\frac{d\xi_a}{dt} + \xi_a\frac{d}{dt}\left(\alpha\frac{\partial\theta}{\partial z}\right). \tag{3}$$

Hence, the generation of potential vorticity is related to the generation of the vertical component of absolute vorticity and latent heat release.

Recall that the equation governing the Ertel PV (e.g., see Chen and Yau 2001) is

$$\frac{d\mathrm{PV}}{dt} = \alpha(\boldsymbol{\eta}\cdot\boldsymbol{\nabla}Q + \boldsymbol{\nabla}\times\mathbf{F}\cdot\boldsymbol{\nabla}\theta), \tag{4}$$

where Q is the diabatic heating rate and $\mathbf{F}$ is the friction vector. The first term on the right is the rate of generation of PV by diabatic heating (mostly latent heating). Its magnitude is much larger than the second term at an altitude of 1.24 km. Figure 13e shows that the rate of PV generation by latent heating is asymmetric, particularly in regions of spiral rainbands around $x = 20$ km and $y = 50$ km. However, its pattern is generally in phase with that of PV, similar to the finding of Chen and Yau (2001). This phase relation between PV and PV generation implies that spiral bands of PV are triggered by moist processes at this level of the troposphere. The same remark also applies to the vertical component of the absolute vorticity by virtue of Eq. (3).

Returning to the azimuthal momentum budget, we display in Fig. 14 the six terms in Eq. (2). Note that the contour intervals are not the same in all the panels. They range from 0.05 m s^{-2} in Figs. 14a–c to 0.02 m s^{-2} in Figs. 14d–f. The quasi-Lagrangian tendency following the azimuthal flow (Fig. 14a) exhibits asymmetric distribution of patches of acceleration/deceleration of the azimuthal wind. The acceleration/deceleration is as large as $\pm$0.2 m s^{-2}, so a local wind maximum of several tens of meters per second can be spun up in a time scale of 10 min. Figures 14b and 14c show that the radial advection of angular momentum per unit radius (VVOR) and the VVA terms make the largest contribution to VTOT which peaks in the updraft core. Figure 13f shows that the absolute vorticity component associated with the azimuthal wind is everywhere positive within a radius of 40 km. The radial outflow (inflow) in the southwest (northeast) quadrant (Fig. 13b) causes outward (inward) advection of angular momentum per unit radius (Fig. 14c) and is responsible for the weakening (strengthening) of the azimuthal wind in the quadrant. As shown in Fig. 5, the maximum tangential wind is located below 1 km. The upward transport of azimuthal momentum by the strong updraft in the eyewall leads to a positive contribution to VTOT (Fig. 14b). While the contribution of VPGF is generally smaller (Fig. 14e), it did contribute somewhat to the acceleration of the azimuthal flow in the southwest quadrant. This is consistent with the results shown in Zhang et al. (2001).

At the lowest model level of 40 m, the azimuthal wind still displays wind streaks exceeding 70 m s^{-1} at a radius of 30 km (Fig. 15a). It is interesting to note the discontinuity in the tangential wind coinciding with the PV (around $x = -15$ km in Figs. 15a,c). This feature is consistent with the finding of Emanuel (1997) who showed that the amplification of the swirling flow in a hurricane is strongly frontogenetic and results in frontal collapse at the inner edge of the eyewall. The radial wind relative to the surface is everywhere inward outside the RMW and the maximum inflow corresponds to the maximum radial wind at $z = 1.24$ km. A patch of outward motion, also associated with that at $z = 1.24$ km (cf. Figs. 15b and 13b), occurs in the eye within a distance of 20 km from the center in the southwest quadrant. The general similarity between the patterns of PV (Fig. 15c), ξ_a (Fig. 15d), and η_a (Fig. 15f) still holds. In general, the diabatic PV generation rate (Fig. 15e) is in phase with the PV bands.

In the surface layer, the VTOT term also exhibits small-scale features with acceleration/deceleration up to $\pm$0.2 m s^{-2} (Fig. 16a). Note that in some locations, the acceleration/deceleration patches occur next to each other, suggestive of the interaction of the azimuthal flow with small-scale vorticity. By far the largest contribution to the azimuthal wind change is the radial advection of angular momentum per unit radius (Fig. 16c), which is similar in structure and magnitude to VTOT (Fig. 16a). The maximum in VVOR occurs at the location where the inflow peaks. The pattern of VPGF at 40 m resembles that at 1.24 km, indicating that the azimuthal distribution of mass is similar at these two levels. In contrast to the situation higher up, the frictional dissipation of azimuthal momentum is larger, especially near the eyewall region where the winds are strong. The maximum dissipation rate is around 0.06 m s^{-2}.

Our budget analysis therefore reveals a possible mechanism for the formation of small-scale wind streaks during the final fast-deepening stage of the simulated

←

FIG. 13. Horizontal structures of (a) the tangential wind (Vt) at intervals of 5 m s^{-1} with values >70 m s^{-1} in shading, (b) the radial wind (Vr) at intervals of 5 m s^{-1} with positive values in shading, (c) the potential vorticity (PV) at intervals of 20 PVU with values >40 PVU in shading, (d) the vertical component of the absolute vorticity (ξ_a) at intervals of 0.002 s^{-1} with values >0.006 s^{-1} in shading, (e) the PV generation rate due to latent heat release at intervals of 0.1 PVU s^{-1} with values >0.1 PVU s^{-1} in shading, and (f) same as in (d) but without the radial wind component (η_a) at 0630 UTC on the level of 1.24 km. Zero contours have been ignored in (d)–(f). Thick dashed lines denote 20- and 40-km radii.

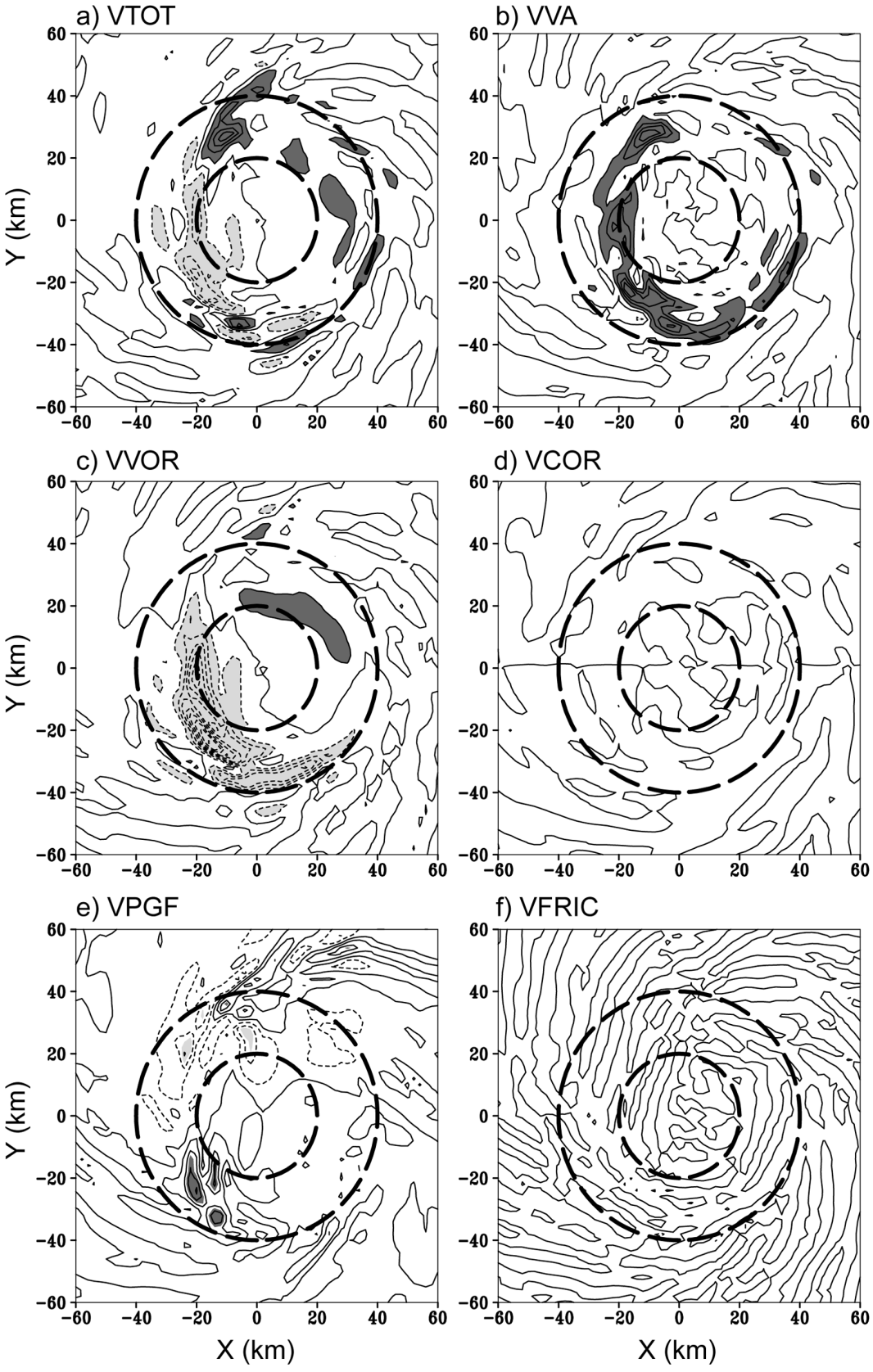
a) VTOT
b) VVA
c) VVOR
d) VCOR
e) VPGF
f) VFRIC
Y (km)
X (km)
60
40
20
0
−20
−40
−60

Hurricane Andrew. Specifically, the quasi-Lagrangian acceleration/deceleration of the azimuthal flow near the surface is related to the radial advection of angular momentum per unit radius, which is in turn associated with η_a. Evidently, ξ_a, η_a, PV, and the PV generation rate from latent heating are correlated. Chen and Yau (2001) has shown that in and above the MBL, vortex Rossby waves interact with friction through Ekman pumping to form upward motion. In a saturated environment, the updrafts release latent heat, and generate positive PV below the level of maximum heating to reinforce the vortex Rossby waves. Thus, PV bands and latent heating feed back onto each other to form spiral bands. In our case, the vorticity associated with the PV generated by latent heating interacts with the environmental flow through the radial advection of angular momentum per unit radius to form small-scale wind streaks. At an altitude of 1.24 km, the effect of the vertical advection of azimuthal momentum becomes important, and results in a positive quasi-Lagrangian acceleration of the azimuthal wind. On the other hand, the radial advection of angular momentum per unit radius contributes both positively and negatively, depending on inflow or outflow. It is mostly the sum of these two effects that causes the small-scale acceleration/deceleration maxima in the azimuthal flow. Even though the VVA term is small at the lowest model level where vertical motion is relatively small, there is a more sizable contribution of vertical advection of azimuthal momentum when integrating over the depth of the MBL (not shown). We remark that in some sense, the mechanism of the formation of wind streaks revealed in our budget calculation bears resemblance to the process of the formation of a midlevel jet in the stratiform region of tropical cyclone rainbands suggested by May (1996). He proposed that these jets may result from PV production by the vertical gradient of heating in the stratiform rain regions in accordance with the analysis of Raymond and Jiang (1990). Willoughby and Black (1996) also pointed out that damaging streaks can be related to the vorticity dynamics of the updrafts. The rapid growth of convective cells locally increases the large background vorticity. We acknowledge that some other processes can also form wind streaks. For example, Montgomery et al. (2002) showed that in the core flow of a vortex in laboratory experiments, mesovortices may also be generated by the instability of the curvilinear shear layer. This possibility should be investigated in high-resolution simulations of real hurricanes in the future.

6. Sensitivity tests on surface fluxes and frictional dissipation

Emanuel (1999) defined potential intensity as the maximum steady intensity a hurricane can achieve based on its energy cycle. By equating the heat input by evaporation from the ocean, multiplied by a thermodynamic efficiency, to the mechanical dissipation in the hurricane's MBL, he obtained an expression of the maximum wind speed as a function of the exchange coefficients for enthalpy and momentum, the absolute temperatures of the sea surface and storm top, and the specific enthalpies of the air at saturation at the ocean surface and the ambient boundary layer. Since there is evidence that the inner-core structures might affect hurricane intensity change (e.g., Chen et al. 2003), it is of interest to explore the impact of changes in surface sensible heat, latent heat, and frictional momentum fluxes, which affect potential intensity, on the inner-core structures and the evolution of the intensity of the hurricane.

The explicit resolution of finescale features in the inner core of Andrew using a 2-km model with sophisticated boundary layer parameterization offers the opportunity for a series of sensitivity tests. Experiments on varying surface friction (F), sensible heat flux (HF), latent heat flux (QF), and removing the Florida peninsula (NoFLO) are performed. These experiments are run for 12 h, similar to the control (Ctrl) run discussed in previous sections.

Table 1 shows the central pressure at the surface (Pmin), the maximum winds (Vmax) and the RMW for the control run and 10 sensitivity experiments after 7 h of integration (valid at 0700 UTC 24 August). These experiments are performed in such a way that the changes in surface friction, sensible heat, and moisture fluxes are independent. For example, in experiment 5F, the surface fluxes are calculated in the same way as the control run, but only the U and V momentum tendencies due to surface friction are artificially increased fivefold in the momentum equations. The heat and moisture fluxes are not directly altered. In experiment 0HF, the surface sensible heat flux is multiplied by zero in the temperature equation but no direct changes are made to the momentum and moisture equations.

An inspection of Table 1 reveals that increasing the surface friction by fivefold (5F) and twofold (2F) results in a weaker storm and more compact cores. In experiment 5F, Pmin is filled by 32 hPa relative to the control, and Vmax and RMW nearly halved. In contrast, reducing or suppressing surface friction (experiments 0.5F

←

FIG. 14. Horizontal structures of individual terms in azimuthal wind budget equation at 0630 UTC on the level of 1.24 km: (a) the Lagrangian tendency (VTOT), (b) the vertical advection (VVA), (c) the radial absolute vorticity flux (VVOR), (d) the Coriolis force on the vertical velocity (VCOR), (e) the pressure gradient force (VPGF), and (f) the friction and diffusion (VFRIC). Contour intervals are (a)–(c) 0.05 m s^{-2} and (d)–(f) 0.02 m s^{-2}. Dark (light) shading indicates regions with values greater (less) than 0.05 m s^{-2} (-0.05 m s^{-2}). Only data inside the 60-km inner domain are plotted. Thick dashed lines denote 20- and 40-km radii.

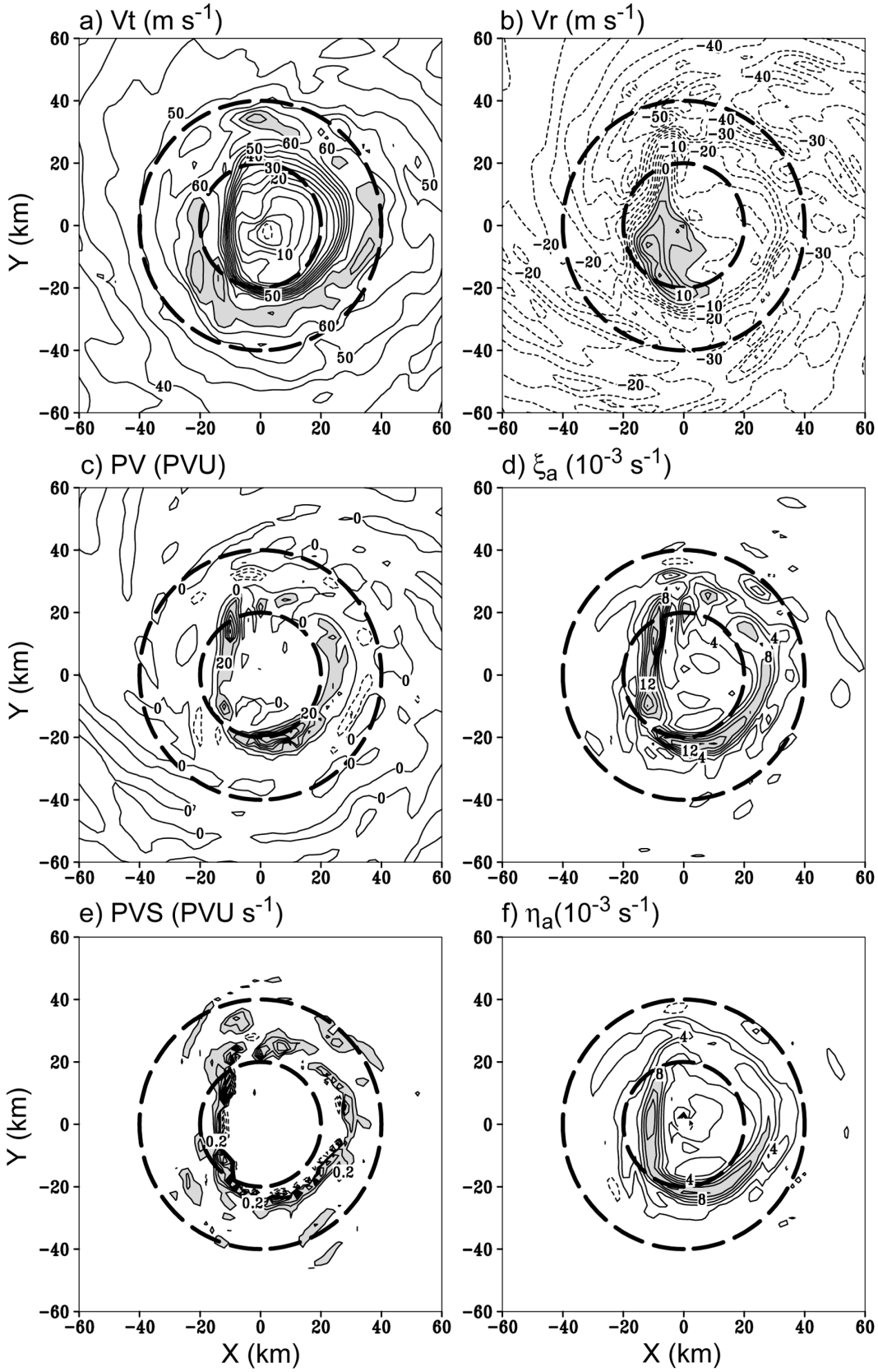

FIG. 15. Same as in Fig. 13 but (a) values >65 m s^{-1} in shading, (c) at intervals of 10 PVU with values >10 PVU in shading, (d) with values >0.008 s^{-1} in shading, and (f) on the lowest model level.

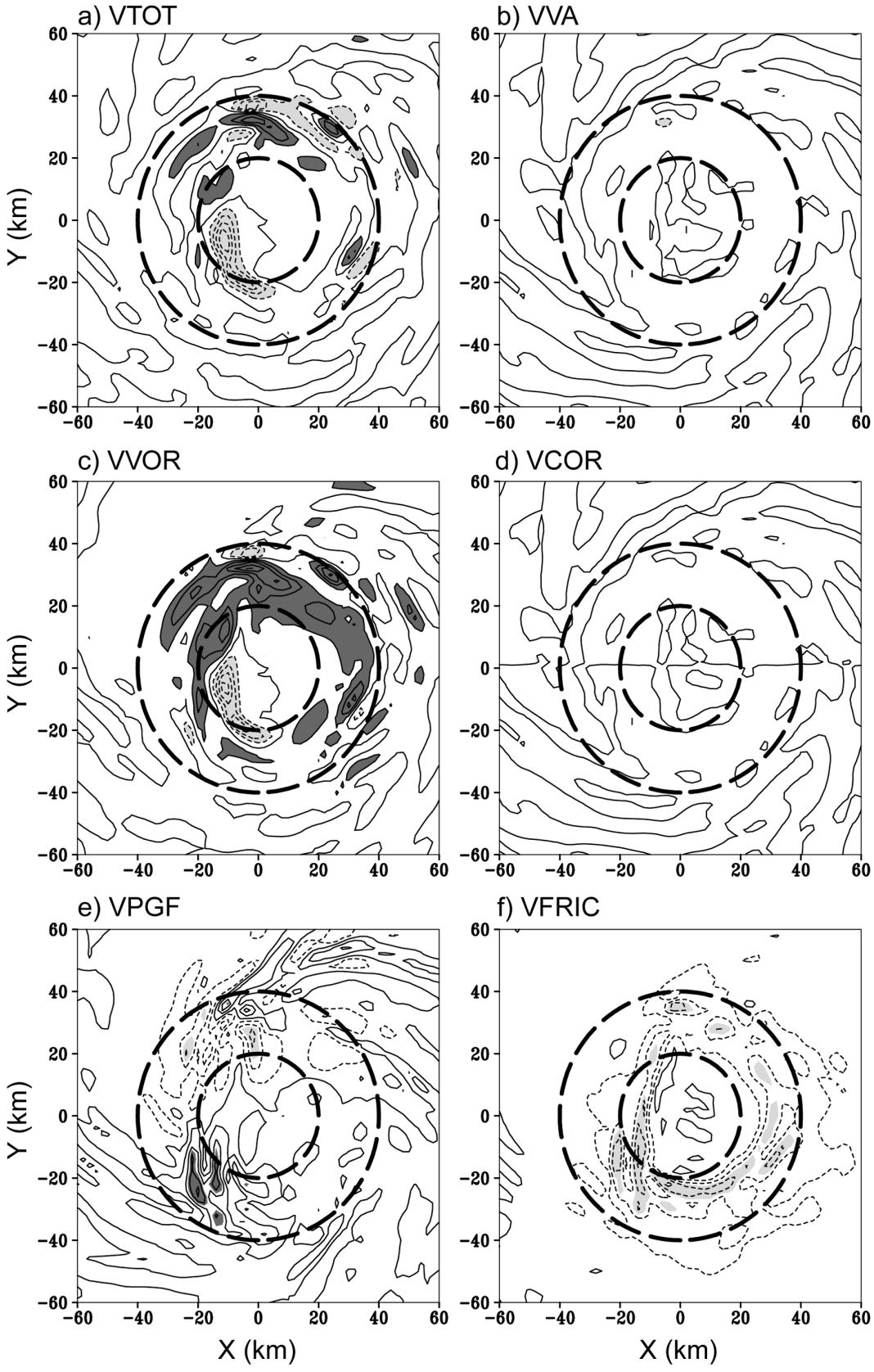

FIG. 16. Same as in Fig. 14 but on the lowest model level.

TABLE 1. Comparison of the control and sensitivity experiments at 0700 UTC 24 Aug 1992.

	Ctrl	5F	2F	0.5F	0F	0.5QF	0.2QF	0QF	0QH	0HF	NoFLO
Pmin (hPa)	919	951	933	908	908	927	935	940	944	922	919
Vmax (m s^{-1})	81.5	48.0	69.5	95.5	106.0	71.0	68.5	62.0	59.5	75.5	68.0
RMW (km)	31	18	30	33	42	32	32	32	32	34	32

and 0F) leads to stronger winds and larger cores. In agreement with many previous studies, reducing the surface moisture and sensible heat supplies results in a weaker storm in terms of both surface pressure and maximum wind. However, the size of the vortex, as measured by the RMW, is almost unchanged. For example, when surface moisture and sensible heat fluxes are completely turned off in experiment 0QH, the modeled storm is 25 hPa and 22 m s^{-1} weaker than the control, whereas its RMW is essentially the same.

Although all the simulated hurricanes respond to the changes in momentum and heat fluxes at the end of 7 h, there are different characteristics of responses. Figure 17 depicts the evolution of *P*min, the maximum wind *at the surface* (WINDmax), and RMW for selected experiments every 20 min. Evidently, the results from the friction experiments diverge most from the control. Although there is no frictional convergence in experiment 0F, the storm deepens on account of the heat and moisture fluxes. The 0F hurricane exhibits the largest wind speed, lowest surface pressure, and largest RMW; while run 5F indicates the opposite. Of interest is that the circulation and intensity of the storm respond very rapidly to the changes in momentum loss through surface friction. In contrast, the sudden variation of the surface heat supply modulates the storm in a slower mode. Zhang et al. (2001) showed that in the radial direction, cyclostrophic balance is a good approximation above the MBL in Hurricane Andrew. However, frictional forces become important in the MBL to form a quasi-three-force balance. Since the radial pressure gradient force is determined by the mass field associated with the overall thermodynamic property of the hurricane vortex, it does not change rapidly when surface friction suddenly changes. Thus, any change of surface friction that upsets the three-force balance in the MBL will lead to a rapid adjustment of the wind field towards a new state of dynamic balance. Indeed, Fig. 17b shows that when friction is removed in experiment 0F, surface tangential winds accelerate rapidly to increase the centrifugal force to balance the pressure gradient force. A similar response occurs in experiment 5F but in an opposite direction. Within a short period of 30 min, surface maximum winds increase by 30 m s^{-1} in run 0F and decrease by 14 m s^{-1} in run 5F.

When the surface sensible heat flux is set to zero in the temperature equation (run 0HF) or when the surface latent heat flux is set to zero in the moisture equation (run 0QF), there are no significant changes in WINDmax and *P*min until after 2 h of integration. The reason is that surface heat sources impact the vortex in an indirect way. Latent heat has to be transported upward and transformed into sensible heat to affect the mass field before the wind field adjusts. Also a large part of the latent heating is offset by adiabatic cooling so the process of adjustment would take longer. On comparing the results from 0HF and 0QF, it is clear that latent heat flux exerts a much larger impact. In fact, surface latent heat flux in the eyewall in the control (not shown) can locally at times exceed 2000 J m^{-2}, a value more than 3 times the sensible heat flux. In terms of the RMW at the surface, Fig. 17c indicates no major difference between the control, NoFLO, 0QF, and 0HF experiments until Andrew makes landfall.

After the initial rapid wind adjustment in the sensitivity experiments, the subsequent results are in qualitative agreement with the theory of Emanuel (1995). Without latent heat flux from the ocean, the storm in 0QF fills rapidly. In 10 h, its *P*min increases by 45 hPa (Fig. 17a), and its WINDmax reduces by about 10 m s^{-1} (Fig. 17b). Sensible heat flux alone (experiment 0HF) does not affect WINDmax or the RMW appreciably, although *P*min fills slightly faster. Turning off the surface friction (0F) causes an increase in the kinetic energy of the system because of surface heat fluxes and no dissipation, leading to an intense and large hurricane. Increasing the surface friction (5F) results in the vortex filling continuously. The loss of angular momentum in the MBL results in a gradual reduction of the maximum surface winds (Fig. 17b) and also a reduction of the inertial stability in the eyewall. Inflow air penetrates further into the eye and the RMW shrinks (Fig. 17c).

The interaction of a hurricane with topography is an important topic which will be studied further in the future. Here it suffices to mention that our NoFLO experiment indicates that the Florida peninsula did not affect strongly *P*min and WINDmax until the eye of Andrew reaches the southeast coast of Florida. This result may arise from the low terrain and moist wetland over Florida. After the landfall of the control storm at 0900 UTC, the NoFLO storm continues to deepen, reaching a *P*min of 913 hPa and a surface WINDmax of 72 m s^{-1} at 1200 UTC. In contrast, the control storm fills and spins down after landfall in response to the change in surface properties.

To examine the changes in the inner-core structures of the vortex, the surface radar reflectivities for selected experiments, valid at 0700 UTC, are displayed in Fig. 18. There is no significant difference between Ctrl and 0HF. With no latent heat flux in 0QF, the precipitation and winds (not shown) in the inner-core region are much weaker, although the overall patterns of the eyewall and

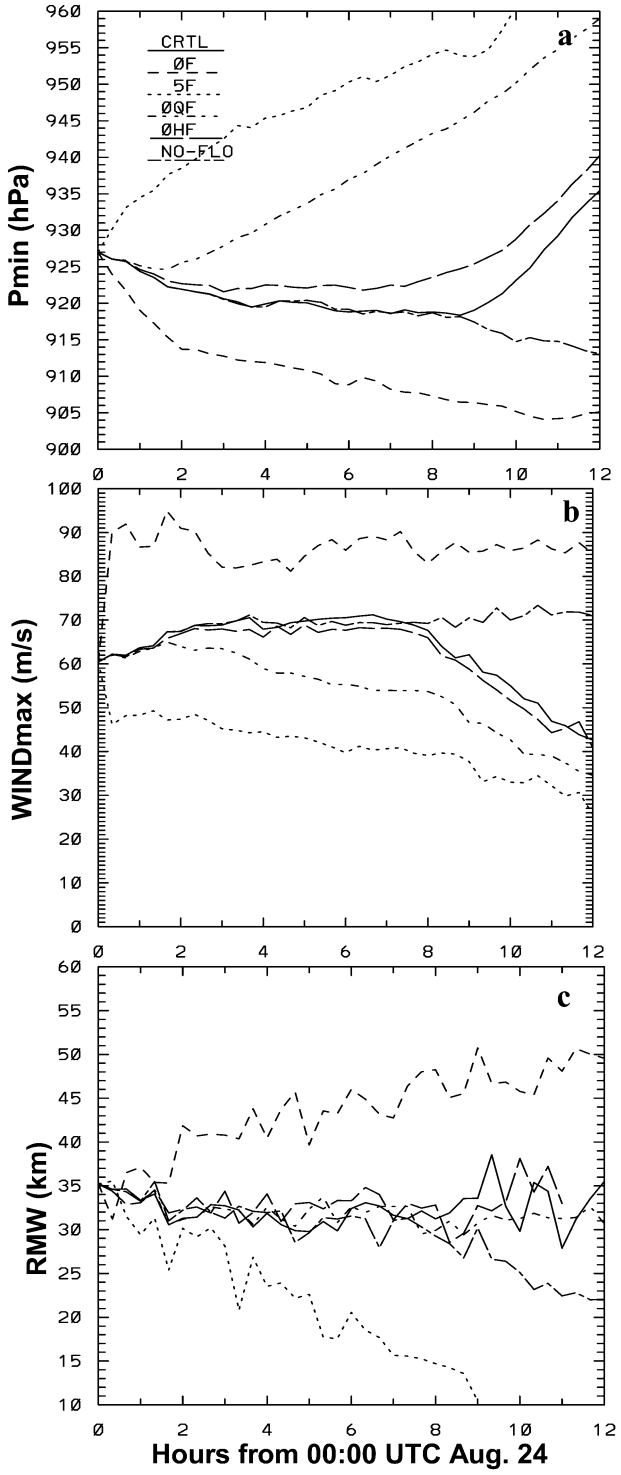

FIG. 17. Comparison of time evolution of (a) minimum pressure (*P*min), (b) maximum winds (WINDmax), and (c) radii of the maximum wind (RMW) of the control simulation (CRTL) and the sensitivity simulations with no surface friction (0F), five-fold surface friction (5F), no surface latent heat flux (0QF), no surface sensible heat flux (0HF), and no Florida peninsular (No_FLO).

spiral bands remain similar to those in Ctrl. In experiment 0F, both the wind and precipitation fields intensify and expand radially outward. The RMW also expands and is located close to the reflectivity maximum at the surface. In the 5F run, a shrinking eye results.

7. Discussion

We have shown that the 2-km run produced finescale features which are in much better agreement with observations than the 6-km simulation. The improved simulation can be explained from recent developments in hurricane dynamics. Emanuel (1997) demonstrated that radial turbulent diffusion of momentum is important in the intensification of hurricanes and argued that the mixing of vorticity between the eyewall and the eye is crucial for a hurricane to reach its maximum intensity. Ample evidence has emerged recently to suggest that the mixing of vorticity can be achieved by vortex Rossby waves (VRWs). In particular, Schubert et al. (1999) used a barotropic model to demonstrate that VRWs can become unstable resulting in the pooling of vorticity from the eyewall into the eye region to form various finescale features including mesovortices, polygonal eyewalls, and asymmetric eye contraction. Kossin and Eastin (2001) analyzed aircraft flight-level data in hurricanes and reported that the tangential wind, angular velocity, and equivalent potential temperature in the eye and eyewall underwent transition consistent with the idea of horizontal vorticity mixing. Chen and Yau (2003) demonstrated that the characteristics of the VRWs, especially their associated eddy momentum and heat transports, evolved in response to the evolution of the structure of the ring of PV forced by latent heating. The VRWs interact with the mean flow and exert a significant impact on the tangential wind of a hurricane.

In a 2-km model, convection is much better resolved. Since the structure of the PV ring in a hurricane is mainly forced by convective heating, it follows that the PV structure and the radial PV gradient would be much better simulated, as would the characteristics of the VRWs and the nonlinear PV mixing. Therefore, the finescale features, which depend crucially on the mixing of vorticity, are expected to be more realistic in the 2-km model than in the 6-km model. As VRWs affect the intensity and the structure of a hurricane, an important ramification is that to properly simulate its detailed dynamics, a grid size of 2 km or less should be employed. In addition to the higher resolution, the scale of the vortex in the initial conditions should also be improved. We have shown that by using a 2-km grid length, the RMW is reduced by 10–20 km from a 6-km simulation, but it is still too large by 20–25 km. We recognize that there are certain limitations to the bogus vortex technique of LZY97. Specifically, the size of the bogus vortex may be larger than the actual vortex because of the coarse resolution involved in its construction. Other

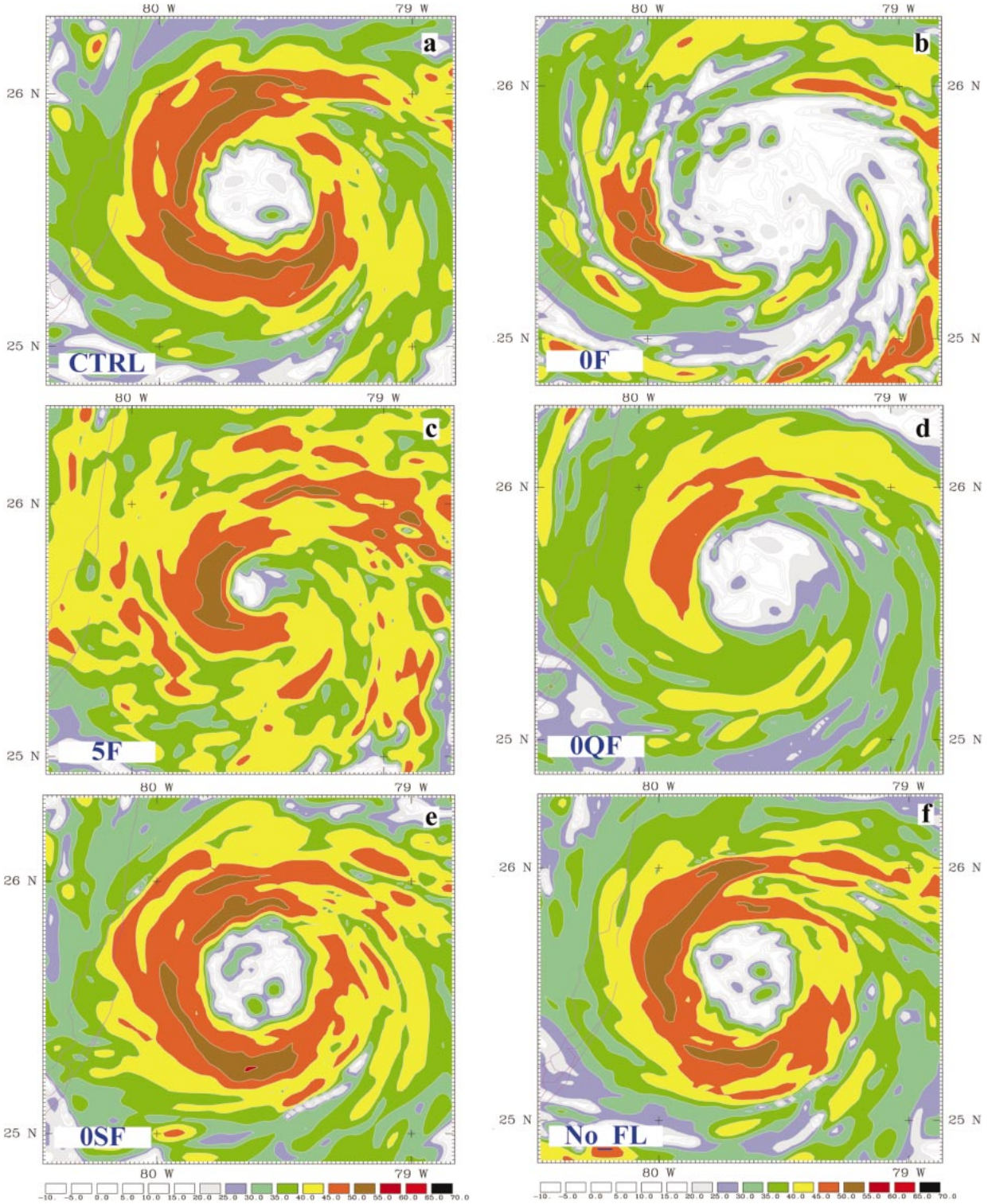

FIG. 18. Same as in Fig. 17, but for the radar reflectivity at the lowest model level, valid at 0700 UTC 24 Aug 1992.

techniques should be tested in the future to improve the specification of the initial vortex.

In our sensitivity experiments, we have shown that changing the surface momentum flux alone produces the largest impact compared to changing the surface heat or moisture fluxes. These results seem to contradict some previous studies, particularly those of Tuleya (1994). He found that the main reason for the weakening of a hurricane on landfall is the finite heat capacity and conductivity of the soil subsurface over land. This leads to a cool pool of surface air and ground temperature beneath the track of the landfalling storm. This low-level cooling strongly impeded evaporation rates beneath the landfalling disturbance and is the major reason for storm weakening. Although not a necessary cause for storm decay, increasing surface roughness and reducing relative wetness do contribute to the enhanced decay.

At the onset, we stated that the differences between our results and those of Tuleya (1994) are mainly caused by different experimental designs and the fact that our hurricane has a more compact eye and much stronger winds. In Tuleya's experiments, surface roughness was varied which impacts on frictional velocity and affects directly the surface fluxes of momentum, heat, and moisture at the same time. For example, when roughness length increases, frictional velocity also increases. Surface friction becomes larger to weaken the storm but surface heat and moisture fluxes increase to counteract the weakening. As a result, the net effect on storm intensity change would be much smaller than if surface momentum flux were changed alone. In contrast, in our experiments, we change the surface fluxes by multiplying the surface flux tendency for either momentum, heat, or moisture by a constant in the respective predictive equation. The tendency for only one of the three quantities is changed in a specific experiment and the other two surface flux tendencies are left unchanged. As a result, the counteracting effect of the heat and moisture fluxes on the momentum change was indirect and much smaller in our case. For instance, Fig. 17b shows that before landfall, experiment 0F indicates a strengthening of the maximum surface wind but experiment 0QF depicts a weakening of the same quantity relative to the control run. The net effect on the surface wind change should be some combination of the effects in these two experiments and would be much smaller than what is indicated in each individual case.

During the landfall stage, the largest difference in the *rate of decrease* of surface maximum wind speed is between experiments NoFLO and the control (Fig. 17b). Since land is removed, the NoFLO experiment essentially represents the development of the hurricane over water throughout the duration of the model integration. Thus, the main reason for the decay of the hurricane is the change of surface properties. Note also that the rates of decrease of the maximum surface wind in experiments 0HF, 0QF, 5F, and the control are not dramatically different after landfall at around 0900 UTC 24 August. These results indicate that after landfall, the surface fluxes of sensible and latent heat are already small so that the effects of further decreases in these fluxes are not significant. Additional increase in momentum flux in experiment 5F also brings about a small effect, showing that a larger surface friction over land enhances the landfall decay process of a hurricane, in agreement with the results of Tuleya (1994). However, in view of the more compact eye and the much stronger winds in Hurricane Andrew, the effect of surface friction is larger in our case than in Tuleya's.

We have also shown that the adjustment of the maximum surface wind occurs faster in the experiments where surface momentum fluxes are altered than in the runs where either surface heat or moisture flux is changed. The reason for the different rates of adjustment can be obtained more quantitatively as follows. According to Holton (1965), the time scale of momentum adjustment τ in the Ekman layer of a rotating vortex is $\tau = (H^2/2\omega\kappa)^{0.5}$, where H is the depth of the Ekman layer, ω is the angular velocity, and κ is the eddy diffusion coefficient. The time scale of adjustment for heat and moisture in the boundary layer by eddy diffusion processes can also be approximated by the same time scale. For $H = 1$ km and $\eta = 10^{-3}$ s^{-1}, κ turns out to be of the order of 50 m^2 s^{-1}. Using a vortex angular velocity $\omega = 2 \times 10^{-3}$ s^{-1}, τ is about 2200 s and is consistent with the time scale of adjustment of maximum surface wind at the start of the simulation in Fig. 17b. In addition to this time scale, changes in surface heat and moisture fluxes would need some additional time to change the mass distribution before these fluxes can effect a surface wind change. The additional time scale is the time required to change the secondary circulation, and can be estimated as the time of geostrophic adjustment of the vortex, or the time for internal gravity waves to travel through the local Rossby radius of deformation. Using an internal gravity wave speed $C_g = NH/\pi$, and the local Rossby radius of deformation $L_R \sim NH/\eta$ with η being the absolute vorticity, the geostrophic adjustment time scale becomes $L_R/C_g = \pi/\eta$ and is about 3000 s for $\eta = 10^{-3}$ s^{-1}. In short, the estimated time scale for surface wind change is about 0.5 h from surface momentum change and is at least 1.5 h from surface heat and moisture flux change. These estimates are in agreement with the results presented in Fig. 17b.

8. Summary and conclusions

In this paper, we extended the results of LZY97 to include explicit simulation of convection and rainbands in the inner-core region employing a cloud-resolving grid size of 2 km. The model is integrated for 12 h from 0000 to 1200 UTC 24 August 1992, a period which covers the final fast-deepening stage and the landfall stage over Florida of Hurricane Andrew. The results

show that the thermodynamic and dynamic structures of the simulated storm in the 2-km run are similar to the coarser-mesh run on the vortex scale. However, there are significant improvements when comparing with radar and other observations. Specifically,

- the eyewall becomes much more compact and symmetric, in better agreement with observations;
- the RMW is reduced by 10–20 km and the width of the eyewall almost decreased by half;
- the model simulates small-scale wind streaks associated with convective cores near the eyewall region; these streaks significantly disturb the zone of maximum surface wind on the vortex scale; and
- the number, intensity, and thermodynamic properties of the spiral rainbands are much better resolved.

Further analysis indicates that improvements in the inner-core structures of the storm are associated with more realistic description of the complex interaction between the vortex-scale dynamics and the convective motion. The strongest convection with a life cycle of <30 min is located in the eyewall and a very strong PV zone formed along the eye–eyewall interface in the deep troposphere. The ring of maximum PV is located in regions of maximum upward motion in the eyewall.

An azimuthal momentum budget is computed to shed light on the formation of small-scale wind streaks. Our analysis indicates that during the final fast-deepening stage of the simulated Andrew, small-scale Lagrangian acceleration/deceleration of the azimuthal flow near the surface is related to the radial advection of angular momentum per unit radius. In turn, the relative vorticity of the azimuthal wind involved in the advection was found to correlate well with the total absolute vorticity, PV, and the PV generation rate from latent heating. At an altitude of 1.24 km, it is the sum of the vertical advection of azimuthal momentum and the radial advection of angular momentum per unit radius that causes the small-scale acceleration/deceleration maxima in the azimuthal flow.

Sensitivity studies are performed by artificially changing the surface friction, moisture, and sensible heat fluxes. It is found that by artificially changing the surface friction *alone* over the ocean impacts most the structure, size, and intensity of the modeled hurricanes. Furthermore, an initial change in surface momentum flux produces a more rapid adjustment in the structure and intensity of the storms than initial changes in surface moisture and heat fluxes.

Acknowledgments. This research was supported by the Canadian Foundation for Climate and Atmospheric Science, the Natural Sciences and Engineering Research Council of Canada, NSF Grant ATM-9802391, NASA Grant NAG-57842, and ONR Grant N00014-96-1-0746.

REFERENCES

Barnes, G. M., and M. D. Powell, 1995: Evolution of the inflow boundary layer of Hurricane Gilbert (1988). *Mon. Wea. Rev.,* **123,** 2348–2368.

Braun, S. A., 2002: A cloud-resolving simulation of Hurricane Bob (1991): Storm structure and eyewall buoyancy. *Mon. Wea. Rev.,* **130,** 1573–1592.

Burk, S. D., and W. T. Thompson, 1989: A vertically nested regional numerical weather prediction model with second-order closure physics. *Mon. Wea. Rev.,* **117,** 2305–2324.

Chen, Y., and M. K. Yau, 2001: Spiral bands in a simulated hurricane. Part I: Vortex Rossby wave verification. *J. Atmos. Sci.,* **58,** 2128–2145.

——, and ——, 2003: Asymmetric structures in a simulated landfalling hurricane. *J. Atmos. Sci.,* **60,** 2294–2312.

——, G. Brunet, and M. K. Yau, 2003: Spiral bands in a simulated hurricane. Part II: Wave activity diagnostics. *J. Atmos. Sci.,* **60,** 1239–1256.

Emanuel, K. A., 1995: Sensitivity of tropical cyclones to surface exchange coefficients and a revised steady-state model incorporating eye dynamics. *J. Atmos. Sci.,* **52,** 3969–3976.

——, 1997: Some aspects of hurricane inner-core dynamics and energetics. *J. Atmos. Sci.,* **54,** 1014–1026.

——, 1999: Thermodynamic control of hurricane intensity. *Nature,* **401,** 665–669.

Gall, R., J. Tuttle, and P. Hildebrand, 1998: Small-scale spiral bands observed in Hurricanes Andrew, Hugo, and Erin. *Mon. Wea. Rev.,* **126,** 1749–1766.

Guinn, T. A., and W. H. Schubert, 1993: Hurricane spiral bands. *J. Atmos. Sci.,* **50,** 3380–3403.

Holland, G. J., 1997: The maximum potential intensity of tropical cyclones. *J. Atmos. Sci.,* **54,** 2519–2541.

Holton, J. R., 1965: The influence of viscous boundary layers on transient motions in a stratified rotating fluid. Part I. *J. Atmos. Sci.,* **22,** 402–411.

Kossin, J. P., and M. D. Eastin, 2001: Two distinct regimes in the kinematic and thermodynamic structure of the hurricane eye and eyewall. *J. Atmos. Sci.,* **58,** 1079–1090.

Kurihara, Y., 1976: On the development of spiral bands in a tropical cyclone. *J. Atmos. Sci.,* **33,** 940–958.

Liu, Y., D.-L. Zhang, and M. K. Yau, 1997: A multiscale study of Hurricane Andrew (1992). Part I: Explicit simulation and verification. *Mon. Wea. Rev.,* **125,** 3073–3093.

——, ——, and ——, 1999: A multiscale numerical study of Hurricane Andrew (1992). Part II: Kinematics and inner-core structures. *Mon. Wea. Rev.,* **127,** 2597–2616.

MacDonald, N. J., 1968: The evidence for the existence of Rossby-like waves in the hurricane vortex. *Tellus,* **20,** 138–150.

Marks, F. D., and R. A. Houze, 1987: Inner core structure of Hurricane Alicia from airborne Doppler radar observations. *J. Atmos. Sci.,* **44,** 1296–1317.

——, ——, and J. F. Gamache, 1992: Dual-aircraft investigation of the inner core of Hurricane Norbert. Part I: Kinematic structure. *J. Atmos. Sci.,* **49,** 919–942.

May, P. T., 1996: The organization of convection in the rainbands of Tropical Cyclone Laurence. *Mon. Wea. Rev.,* **124,** 807–815.

Mayfield, M., L. Avila, and E. N. Rappaport, 1994: Atlantic hurricane season of 1992. *Mon. Wea. Rev.,* **122,** 517–538.

Montgomery, M. T., and R. J. Kallenbach, 1997: A theory for vortex Rossby-waves in its application to spiral bands and intensity changes of hurricanes. *Quart. J. Roy. Meteor. Soc.,* **123,** 435–465.

——, V. A. Vladimirov, and P. V. Denissenko, 2002: An experimental study on hurricane mesovortices. *J. Fluid Mech.,* **471,** 1–32.

Powell, M. D., and S. H. Houston, 1996: Hurricane Andrew's landfall in south Florida. Part II: Surface wind fields and potential real-time applications. *Wea. Forecasting,* **11,** 329–349.

——, P. P. Dodge, and M. L. Black, 1991: The landfall of Hurricane

Hugo in the Carolinas: Surface wind distribution. *Wea. Forecasting,* **6,** 379–399.
Pu, Z.-X., and S. A. Braun, 2001: Evaluation of bogus vortex techniques with four-dimensional variational data assimilation. *Mon. Wea. Rev.,* **129,** 2023–2039.
Raymond, D. J., and H. Jiang, 1990: A theory for long-lived mesoscale convective systems. *J. Atmos. Sci.,* **47,** 3067–3077.
Reasor, P. D., M. T. Montgomery, F. D. Marks, and J. F. Gamache, 2000: Low-wavenumber structure and evolution of the hurricane inner core observed by airborne dual-Doppler radar. *Mon. Wea. Rev.,* **128,** 1653–1680.
Schubert, W. H., M. T. Montgomery, R. K. Taft, T. A. Guinn, S. R. Fulton, J. P. Kossin, and J. P. Edwards, 1999: Polygonal eyewalls, asymmetric eye contraction, and potential vorticity mixing in hurricanes. *J. Atmos. Sci.,* **56,** 1197–1223.
Tao, W.-K., and J. Simpson, 1993: The Goddard Cumulus Ensemble Model. Part I: Model description. *Terr. Atmos. Oceanic Sci.,* **4,** 35–72.
Tuleya, R. E., 1994: Tropical storm development and decay: Sensitivity to surface boundary conditions. *Mon. Wea. Rev.,* **122,** 291–304.
Wakimoto, R. M., and P. G. Black, 1994: Damage survey of Hurricane Andrew and its relationship to the eyewall. *Bull. Amer. Meteor. Soc.,* **75,** 189–200.
Wang, Y., 2002a: Vortex Rossby waves in a numerically simulated tropical cyclone. Part I: Overall structure, potential vorticity, and kinetic energy budgets. *J. Atmos. Sci.,* **59,** 1213–1238.
——, 2002b: Vortex Rossby waves in a numerically simulated tropical cyclone. Part II: The role in tropical cyclone structure and intensity changes. *J. Atmos. Sci.,* **59,** 1239–1262.
Willoughby, H. E., 1978a: A possible mechanism for the formation of hurricane rainbands. *J. Atmos. Sci.,* **35,** 838–848.
——, 1978b: The vertical structure of hurricane rainbands and their interaction with the mean vortex. *J. Atmos. Sci.,* **35,** 849–858.
——, 1998: Tropical cyclone eye thermodynamics. *Mon. Wea. Rev.,* **126,** 3053–3067.
——, and P. G. Black, 1996: Hurricane Andrew in Florida: Dynamics of a disaster. *Bull. Amer. Meteor. Soc.,* **77,** 543–652.
Zhang, D.-L., and X. Wang, 2003: Dependence of hurricane intensity and structures on vertical resolution and time-step size. *Adv. Atmos. Sci.,* **20,** 711–725.
——, Y. Liu, and M. K. Yau, 1999: Surface winds at landfall of Hurricane Andrew (1992)—A reply. *Mon. Wea. Rev.,* **127,** 1711–1721.
——, ——, and ——, 2000: A multiscale numerical study of Hurricane Andrew (1992). Part III: Dynamically induced vertical motion. *Mon. Wea. Rev.,* **128,** 3772–3788.
——, ——, and ——, 2001: A multiscale numerical study of Hurricane Andrew (1992). Part IV: Unbalanced flow. *Mon. Wea. Rev.,* **129,** 92–107.
——, ——, and ——, 2002: A multiscale numerical study of Hurricane Andrew (1992). Part V: Inner-core thermodynamics. *Mon. Wea. Rev.,* **130,** 2745–2763.
Zhu, T., D.-L. Zhang, and F. Weng, 2002: Impact of the Advanced Microwave Sounding Unit measurements on hurricane prediction. *Mon. Wea. Rev.,* **130,** 2416–2431.